

# Chapter 2

## Feedback Control of Particle Size Distribution in Nanoparticle Synthesis and Processing

Mingheng Li and Panagiotis D. Christofides

### 2.1 Introduction

Particulate processes (also known as dispersed-phase processes) are characterized by the co-presence of and strong interaction between a continuous (gas or liquid) phase and a particulate (dispersed) phase and are essential in making many high-value industrial products. Particulate processes play a prominent role in a number of process industries since about 60% of the products in the chemical industry are manufactured as particulates with an additional 20% using powders as ingredients. Representative examples of particulate processes for micro- and nano-particle synthesis and processing include the crystallization of proteins for pharmaceutical applications [2], the emulsion polymerization of nano-sized latex particles [50], the aerosol synthesis of nanocrystalline catalysts [64], and thermal spray processing of nanostructured functional thermal barrier coatings to protect turbine blades [1]. The industrial importance of particulate processes and the realization that the physicochemical and mechanical properties of materials made with particulates depend heavily on the characteristics of the underlying particle-size distribution (PSD) have motivated significant research attention over the last ten years on model-based control of particulate processes. These efforts have also been complemented by recent and ongoing developments in measurement technology which allow the accurate and fast online measurement of key process variables including important characteristics of PSDs (e.g., [37,55,56]). The recent efforts on model-based control

---

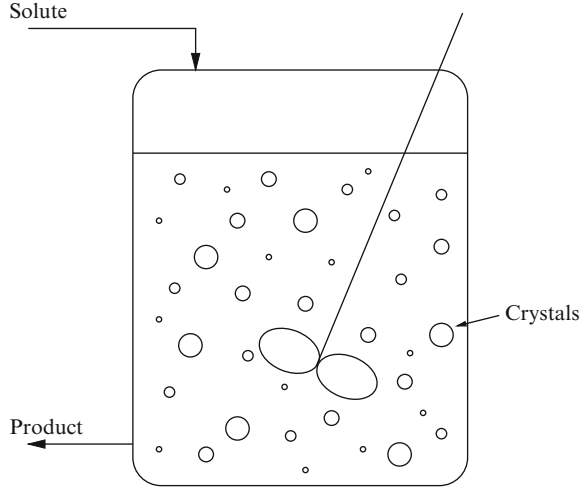
M. Li (✉)

Department of Chemical and Materials Engineering, California State  
Polytechnic University, Pomona, CA 91768, USA  
e-mail: [minghengli@csupomona.edu](mailto:minghengli@csupomona.edu)

P.D. Christofides

Department of Chemical and Biomolecular Engineering, University of California,  
Los Angeles, CA 90095, USA  
e-mail: [pdc@seas.ucla.edu](mailto:pdc@seas.ucla.edu)

**Fig. 2.1** Schematic of a continuous crystallizer



of particulate processes have also been motivated by significant advances in the physical modeling of highly coupled reaction-transport phenomena in particulate processes that cannot be easily captured through empirical modeling. Specifically, population balances have provided a natural framework for the mathematical modeling of PSDs in broad classes of particulate processes (see, for example, the tutorial article [30] and the review article [54]), and have been successfully used to describe PSDs in emulsion polymerization reactors (e.g., [13, 15]), crystallizers (e.g., [4, 55]), aerosol reactors (e.g., [23]), and cell cultures (e.g., [12]). To illustrate the structure of the mathematical models that arise in the modeling and control of particulate processes, we focus on three representative examples: continuous crystallization, batch crystallization, and aerosol synthesis.

### 2.1.1 Continuous Crystallization

Crystallization is a particulate process, which is widely used in industry for the production of many micro- or nano-sized products including fertilizers, proteins, and pesticides. A typical continuous crystallization process is shown in Fig. 2.1. Under the assumptions of isothermal operation, constant volume, well-mixed suspension, nucleation of crystals of infinitesimal size and mixed product removal, a dynamic model for the crystallizer can be derived from a population balance for the particle phase and a mass balance for the solute concentration and has the following mathematical form [32, 39]:

$$\begin{aligned} \frac{\partial n(r,t)}{\partial t} &= -\frac{\partial(R(t)n(r,t))}{\partial r} - \frac{n(r,t)}{\tau} + \delta(r-0)Q(t), \\ \frac{dc(t)}{dt} &= \frac{(c_0 - \rho)}{\varepsilon(t)\tau} + \frac{(\rho - c(t))}{\tau} + \frac{(\rho - c(t))}{\varepsilon(t)} \frac{d\varepsilon(t)}{dt}, \end{aligned} \quad (2.1)$$

where  $n(r, t)dr$  is the number of crystals in the size range of  $[r, r + dr]$  at time  $t$  per unit volume of suspension,  $\tau$  is the residence time,  $\rho$  is the density of the crystal,  $c(t)$  is the solute concentration in the crystallizer,  $c_0$  is the solute concentration in the feed, and

$$\varepsilon(t) = 1 - \int_0^\infty n(r, t) \frac{4}{3} \pi r^3 dr$$

is the volume of liquid per unit volume of suspension.  $R(t)$  is the crystal growth rate,  $\delta(r - 0)$  is the standard Dirac function, and  $Q(t)$  is the crystal nucleation rate. The term  $\delta(r - 0)Q(t)$  accounts for the production of crystals of infinitesimal (zero) size via nucleation. An example of expressions of  $R(t)$  and  $Q(t)$  is the following:

$$R(t) = k_1(c(t) - c_s), \quad Q(t) = \varepsilon(t)k_2 e^{-\frac{k_3}{(c(t)/c_s - 1)^2}}, \quad (2.2)$$

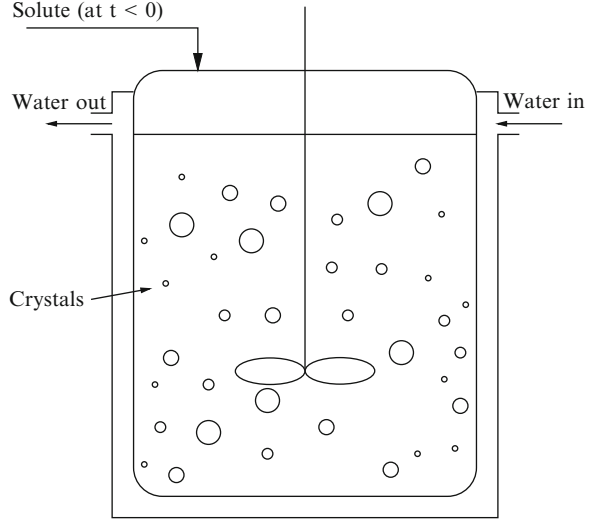
where  $k_1$ ,  $k_2$ , and  $k_3$  are constants and  $c_s$  is the concentration of solute at saturation. For a variety of operating conditions (see [6] for model parameters and detailed studies), the continuous crystallizer model of (2.1) exhibits highly oscillatory behavior (the main reason for this behavior is that the nucleation rate is much more sensitive to supersaturation relative to the growth rate – i.e., compare the dependence of  $R(t)$  and  $Q(t)$  on the values of  $c(t)$  and  $c_s$ ), which suggests the use of feedback control to ensure stable operation and attain a crystal size distribution (CSD) with desired characteristics. To achieve this control objective, the inlet solute concentration can be used as the manipulated input and the crystal concentration as the controlled and measured output.

### 2.1.2 Batch Protein Crystallization

Batch crystallization plays an important role in the pharmaceutical industry. We consider a batch crystallizer, which is used to produce tetragonal HEW (hen-egg-white) lysozyme crystals from a supersaturated solution [62]. A schematic of the batch crystallizer is shown in Fig. 2.2. Applying population, mass and energy balances to the process, the following mathematical model is obtained:

$$\begin{aligned} \frac{\partial n(r, t)}{\partial t} + G(t) \frac{\partial n(r, t)}{\partial r} &= 0, \quad n(0, t) = \frac{B(t)}{G(t)}, \\ \frac{dC(t)}{dt} &= -24\rho k_v G(t) \mu_2(t), \\ \frac{dT(t)}{dt} &= -\frac{UA}{MC_p} (T(t) - T_j(t)), \end{aligned} \quad (2.3)$$

**Fig. 2.2** Schematic of a batch cooling crystallizer



where  $n(r,t)$  is the CSD,  $B(t)$  is the nucleation rate,  $G(t)$  is the growth rate,  $C(t)$  is the solute concentration,  $T(t)$  is the crystallizer temperature,  $T_j(t)$  is the jacket temperature,  $\rho$  is the density of crystals,  $k_v$  is the volumetric shape factor,  $U$  is the overall heat-transfer coefficient,  $A$  is the total heat-transfer surface area,  $M$  is the mass of solvent in the crystallizer,  $C_p$  is the heat capacity of the solution, and  $\mu_2(t) = \int_0^\infty r^2 n(r,t) dr$  is the second moment of the CSD. The nucleation rate,  $B(t)$ , and the growth rate,  $G(t)$ , are given by [62]:

$$B(t) = k_a C(t) \exp\left(-\frac{k_b}{\sigma^2(t)}\right), \quad G(t) = k_g \sigma^g(t), \quad (2.4)$$

where  $\sigma(t)$ , the supersaturation, is a dimensionless variable and is defined as  $\sigma(t) = \ln(C(t)/C_s(T(t)))$ ,  $C(t)$  is the solute concentration,  $g$  is the exponent relating growth rate to the supersaturation, and  $C_s(T)$  is the saturation concentration of the solute, which is a nonlinear function of the temperature of the form:

$$C_s(T) = 1.0036 \times 10^{-3} T^3 + 1.4059 \times 10^{-2} T^2 - 0.12835 T + 3.4613. \quad (2.5)$$

The existing experimental results [68] show that the growth condition of tetragonal HEW lysozyme crystal is significantly affected by the supersaturation. Low supersaturation will lead to the cessation of the crystal growth. On the other hand, rather than forming tetragonal crystals, large amount of needle crystals will form when the supersaturation is too high. Therefore, a proper range of supersaturation is necessary to guarantee the product's quality. The jacket temperature,  $T_j$ , is manipulated to achieve the desired crystal shape and size distribution.

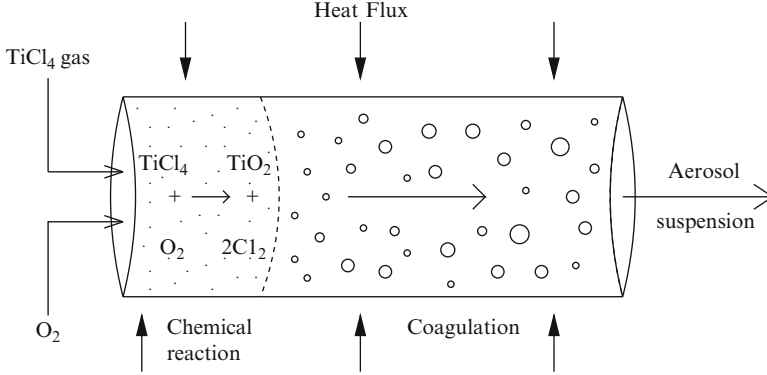


**Fig. 2.3** Schematic of a titania aerosol reactor

### 2.1.3 Aerosol Synthesis

Aerosol processes are increasingly being used for the large-scale production of nano- and micron-sized particles. A typical aerosol flow reactor for the synthesis of titania aerosol with simultaneous chemical reaction, nucleation, condensation, coagulation, and convective transport is shown in Fig. 2.3. A general mathematical model, which describes the spatiotemporal evolution of the particle size distribution in such aerosol processes can be obtained from a population balance and consists of the following nonlinear partial integro-differential equation [33, 34]:

$$\begin{aligned} & \frac{\partial n(v, z, t)}{\partial t} + v_z \frac{\partial n(v, z, t)}{\partial z} + \frac{\partial (G(\bar{x}, v, z) n(v, z, t))}{\partial v} - I(v^*) \delta(v - v^*) \\ &= \frac{1}{2} \int_0^v \beta(v - \bar{v}, \bar{v}, \bar{x}) n(v - \bar{v}, t) n(\bar{v}, z, t) d\bar{v} - n(v, z, t) \int_0^\infty \beta(v, \bar{v}, \bar{x}) n(\bar{v}, z, t) d\bar{v}, \quad (2.6) \end{aligned}$$

where  $n(v, z, t)$  denotes the particle size distribution function,  $v$  is the particle volume,  $t$  is the time,  $z \in [0, L]$  is the spatial coordinate,  $L$  is the length scale of the process,  $v^*$  is the size of the nucleated aerosol particles,  $v_z$  is the velocity of the fluid,  $\bar{x}$  is the vector of the state variables of the continuous phase,  $G(\cdot, \cdot, \cdot)$ ,  $I(\cdot)$ ,  $\beta(\cdot, \cdot, \cdot)$  are nonlinear scalar functions which represent the growth, nucleation, and coagulation rates and  $\delta(\cdot)$  is the standard Dirac function. The model of (2.6) is coupled with a mathematical model, which describes the spatiotemporal evolution of the concentrations of species and temperature of the gas phase ( $\bar{x}$ ) that can be obtained from mass and energy balances. The control problem is to regulate process variables such as inlet flow rates and wall temperature to produce aerosol products with desired size distribution characteristics.

The mathematical models of (2.1), (2.3) and (2.6) demonstrate that particulate process models are nonlinear and distributed parameter in nature. These properties have motivated extensive research on the development of efficient numerical

methods for the accurate computation of their solution (see, for example, [12, 23, 25, 38, 48, 54, 63]). However, in spite of the rich literature on population balance modeling, numerical solution, and dynamical analysis of particulate processes, up to about ten years ago, research on model-based control of particulate processes had been very limited. Specifically, early research efforts had mainly focused on the understanding of fundamental control-theoretic properties (controllability and observability) of population balance models [58] and the application of conventional control schemes (such as proportional-integral and proportional-integral-derivative control, self-tuning control) to crystallizers and emulsion polymerization processes (see, for example, [13, 57, 59] and the references therein). The main difficulty in synthesizing nonlinear model-based feedback controllers for particulate processes is the distributed parameter nature of the population balance models, which does not allow their direct use for the synthesis of low-order (and therefore, practically implementable) model-based feedback controllers. Furthermore, a direct application of the aforementioned solution methods to particulate process models leads to finite dimensional approximations of the population balance models (i.e., nonlinear ordinary differential equation (ODE) systems in time) which are of very high order, and thus inappropriate for the synthesis of model-based feedback controllers that can be implemented in realtime. This limitation had been the bottleneck for model-based synthesis and real-time implementation of model-based feedback controllers on particulate processes.

## 2.2 Model-Based Control of Particulate Processes

### 2.2.1 Overview

Motivated by the lack of population balance-based control methods for particulate processes and the need to achieve tight size distribution control in many particulate processes, we developed, over the last ten years, a general framework for the synthesis of nonlinear, robust, and predictive controllers for particulate processes based on population balance models [6–9, 16, 33, 35, 60, 62]. Specifically, within the developed framework, nonlinear low-order approximations of the particulate process models are initially derived using order reduction techniques and are used for controller synthesis. Subsequently, the infinite-dimensional closed-loop system stability, performance and robustness properties were precisely characterized in terms of the accuracy of the approximation of the low-order models. Furthermore, controller designs were proposed that deal directly with the key practical issues of uncertainty in model parameters, unmodeled actuator/sensor dynamics and constraints in the capacity of control actuators and the magnitude of the process state variables. It is also important to note that owing to the low-dimensional structure of the controllers, the computation of the control action involves the solution of a small set of ODEs, and thus, the developed controllers can be readily

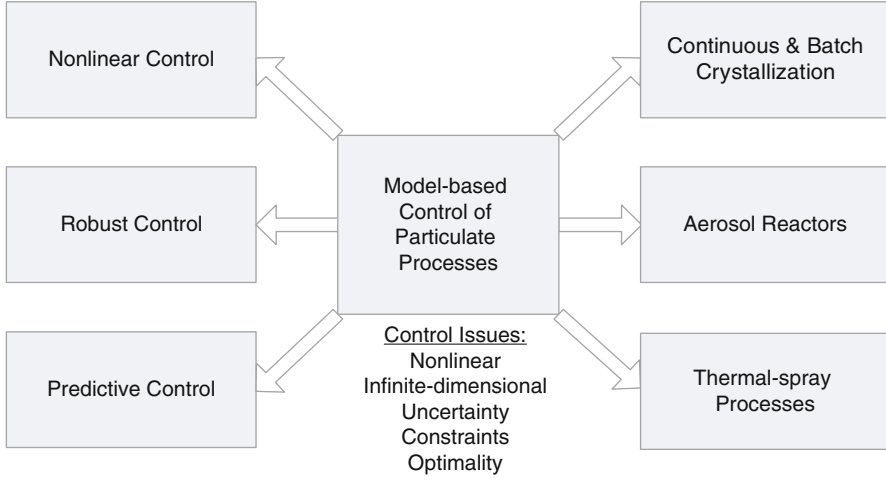


**Fig. 2.4** Summary of our research on model-based control of particulate processes

implemented in realtime with reasonable computing power, thereby resolving the main issue on model-based control of particulate processes. In addition to theoretical developments, we also successfully demonstrated the application of the proposed methods to size distribution control in continuous and batch crystallization, aerosol, and thermal spray processes and documented their effectiveness and advantages with respect to conventional control methods. Figure 2.4 summarizes these efforts. The reader may refer to [4, 12, 15] for recent reviews of results on simulation and control of particulate processes.

### 2.2.2 Particulate Process Model

To present the main elements of our approach to model-based control of particulate processes, we focus on a general class of spatially homogeneous particulate processes with simultaneous particle growth, nucleation, agglomeration, and breakage. Examples of such processes have been introduced in the previous section. Assuming that particle size is the only internal particle coordinate and applying a dynamic material balance on the number of particles of size  $r$  to  $r + dr$  (population balance), we obtain the following general nonlinear partial integro-differential equation, which describes the rate of change of the PSD,  $n(r, t)$ :

$$\frac{\partial n}{\partial t} = -\frac{\partial(G(x, r)n)}{\partial r} + w(n, x, r), \quad (2.7)$$

where  $n(r, t)$  is the particle number size distribution,  $r \in [0, r_{\max}]$  is the particle size, and  $r_{\max}$  is the maximum particle size (which may be infinity),  $t$  is the time and

$x \in \mathbb{R}^n$  is the vector of state variables, which describe properties of the continuous phase (for example, solute concentration, temperature, and pH in a crystallizer); see (2.8) for the system that describes the dynamics of  $x$ .  $G(x, r)$  and  $w(n, x, r)$  are nonlinear scalar functions whose physical meaning can be explained as follows:  $G(x, r)$  accounts for particle growth through condensation and is usually referred to as growth rate. It usually depends on the concentrations of the various species present in the continuous phase, the temperature of the process, and the particle size. On the other hand,  $w(n, x, r)$  represents the net rate of introduction of new particles into the system. It includes all the means by which particles appear or disappear within the system including particle agglomeration (merging of two particles into one), breakage (division of one particle to two) as well as nucleation of particles of size  $r \geq 0$  and particle feed and removal. The rate of change of the continuous-phase variables  $x$  can be derived by a direct application of mass and energy balances to the continuous phase and is given by a nonlinear integro-differential equation system of the general form:

$$\dot{x} = f(x) + g(x)u(t) + A \int_0^{r_{\max}} a(n, r, x) dr, \quad (2.8)$$

where  $f(x)$  and  $a(n, r, x)$  are nonlinear vector functions,  $g(x)$  is a nonlinear matrix function,  $A$  is a constant matrix and  $u(t) = [u_1 \ u_2 \ \cdots \ u_m] \in \mathbb{R}^m$  is the vector of manipulated inputs. The term  $A \int_0^{r_{\max}} a(n, r, x) dr$  accounts for mass and heat transfer from the continuous phase to all the particles in the population (see [8] for details).

### 2.2.3 Model Reduction of Particulate Process Models

While the population balance models are infinite dimensional systems, the dominant dynamic behavior of many particulate process models has been shown to be low dimensional. Manifestations of this fundamental property include the occurrence of oscillatory behavior in continuous crystallizers [32] and the ability to capture the long-term behavior of aerosol systems with self-similar solutions [23]. Motivated by this, we introduced a general methodology for deriving low-order ODE systems that accurately reproduce the dominant dynamics of the nonlinear integro-differential equation system of (2.7) and (2.8) [6]. The proposed model reduction methodology exploits the low-dimensional behavior of the dominant dynamics of the system of (2.7) and (2.8) and is based on a combination of the method of weighted residuals with the concept of approximate inertial manifolds.

Specifically, the proposed approach initially employs the method of weighted residuals (see [54] for a comprehensive review of results on the use of this method for solving population balance equations) to construct a nonlinear, possibly high-order, ODE system that accurately reproduces the solutions and dynamics of the distributed parameter system of (2.7) and (2.8). We first consider an orthogonal



set of basis functions  $\phi_k(r)$ , where  $r \in [0, r_{\max})$ ,  $k = 1, \dots, \infty$ , and expand the particle size distribution function  $n(r, t)$  in an infinite series in terms of  $\phi_k(r)$  as follows:

$$n(r, t) = \sum_{k=1}^{\infty} a_k(t) \phi_k(r), \quad (2.9)$$

where  $a_k(t)$  are time-varying coefficients. In order to approximate the system of (2.7) and (2.8) with a finite set of ODEs, we obtain a set of  $N$  equations by substituting (2.9) into (2.7) and (2.8), multiplying the population balance with  $N$  different weighting functions  $\psi_v(r)$  (that is,  $v = 1, \dots, N$ ), and integrating over the entire particle size spectrum. In order to obtain a finite dimensional model, the series expansion of  $n(r, t)$  is truncated up to order  $N$ . The infinite dimensional system of (2.7) reduces to the following finite set of ODEs:

$$\begin{aligned} \int_0^{r_{\max}} \psi_v(r) \sum_{k=1}^N \phi_k(r) \frac{\partial a_{kN}(t)}{\partial t} dr &= \sum_{k=1}^N a_{kN}(t) \int_0^{r_{\max}} \psi_v(r) \frac{\partial (G(x_N, r) \phi_k(r))}{\partial r} dr, \\ &+ \int_0^{r_{\max}} \psi_v(r) w \left( \sum_{k=1}^N a_{kN}(t) \phi_k(r), x_N, r \right) dr, \quad v = 1, \dots, N \\ \dot{x}_N &= f(x_N) + g(x_N)u(t) + A \int_0^{r_{\max}} a \left( \sum_{k=1}^N a_{kN}(t) \phi_k(r), r, x_N \right) dr, \end{aligned} \quad (2.10)$$

where  $x_N$  and  $a_{kN}$  are the approximations of  $x$  and  $a_k$  obtained by an  $N$ -th order truncation. From (2.10), it is clear that the form of the ODEs that describe the rate of change of  $a_{kN}(t)$  depends on the choice of the basis and weighting functions, as well as on  $N$ . The system of (2.10) was obtained from a direct application of the method of weighted residuals (with arbitrary basis functions) to the system of (2.7) and (2.8), and thus, may be of very high order in order to provide an accurate description of the dominant dynamics of the particulate process model. High-dimensionality of the system of (2.10) leads to complex controller design and high-order controllers, which cannot be readily implemented in practice. To circumvent these problems, we exploited the low-dimensional behavior of the dominant dynamics of particulate processes and proposed an approach based on the concept of inertial manifolds to derive low-order ODE systems that accurately describe the dominant dynamics of the system of (2.10) [6]. This order reduction technique initially employs singular perturbation techniques to construct nonlinear approximations of the modes neglected in the derivation of the finite dimensional model of (2.10) (i.e., modes of order  $N + 1$  and higher) in terms of the first  $N$  modes. Subsequently, these steady-state expressions for the modes of order  $N + 1$  and higher (truncated up to appropriate order) are used in the model of (2.10) (instead of setting them to zero) and significantly improve the accuracy of the model of (2.10) without increasing its dimension; details on this procedure can be found in [6].

It is important to note that the method of weighted residuals reduces to the method of moments when the basis functions are chosen to be Laguerre polynomials

and the weighting functions are chosen as  $\psi_v = r^v$ . The moments of the particle size distribution are defined as:

$$\mu_v = \int_0^\infty r^v n(r,t) dr, \quad v = 0, \dots, \infty \quad (2.11)$$

and the moment equations can be directly generated from the population balance model by multiplying it by  $r^v$ ,  $v = 0, \dots, \infty$  and integrating from 0 to  $\infty$ . The procedure of forming moments of the population balance equation very often leads to terms that may not reduce to moments, terms that include fractional moments, or to an unclosed set of moment equations. To overcome this problem, the particle size distribution may be expanded in terms of Laguerre polynomials defined in  $L_2[0, \infty)$  and the series solution using a finite number of terms may be used to close the set of moment equations (this procedure has been successfully used for models of crystallizers with fine traps used to remove small crystals [7]).

## 2.2.4 Model-Based Control Using Low-Order Models

### 2.2.4.1 Nonlinear Control

Low-order models can be constructed using the techniques described in the previous section. We describe an application to the continuous crystallization process of Sect. 2.1.1. First, the method of moments is used to derive the following infinite-order dimensionless system from (2.1) for the continuous crystallization process:

$$\begin{aligned} \frac{d\tilde{x}_0}{dt} &= -\tilde{x}_0 + (1 - \tilde{x}_3)Da e^{-F/\tilde{y}^2}, \\ \frac{d\tilde{x}_1}{dt} &= -\tilde{x}_1 + \tilde{y}\tilde{x}_0, \\ \frac{d\tilde{x}_2}{dt} &= -\tilde{x}_2 + \tilde{y}\tilde{x}_1, \\ \frac{d\tilde{x}_3}{dt} &= -\tilde{x}_3 + \tilde{y}\tilde{x}_2, \\ \frac{d\tilde{x}_v}{dt} &= -\tilde{x}_v + \tilde{y}\tilde{x}_{v-1}, \quad v = 4, 5, 6, \dots, \\ \frac{d\tilde{y}}{dt} &= \frac{1 - \tilde{y} - (\alpha - \tilde{y})\tilde{y}\tilde{x}_2}{1 - \tilde{x}_3}, \end{aligned} \quad (2.12)$$

where  $\tilde{x}_i$  and  $\tilde{y}$  are the dimensionless  $i$ -th moment and solute concentration, respectively, and  $Da$  and  $F$  are dimensionless parameters [6]. On the basis of the system of (2.12), it is clear that the moments of order four and higher do not affect

those of order three and lower, and moreover, the state of the infinite dimensional system:

$$\frac{d\tilde{x}_v}{dt} = -\tilde{x}_v + \tilde{y}\tilde{x}_{v-1}, \quad v = 4, \dots, \quad (2.13)$$

is bounded when  $x_3$  and  $y$  are bounded, and it converges to a globally exponentially stable equilibrium point when  $\lim_{t \rightarrow \infty} x_3 = c_1$  and  $\lim_{t \rightarrow \infty} \tilde{y} = c_2$ , where  $c_1$  and  $c_2$  are constants. This implies that the dominant dynamics (that is, dynamics associated with eigenvalues that are close to the imaginary axis) of the process of (2.1) can be adequately captured by the following fifth-order moment model:

$$\begin{aligned} \frac{d\tilde{x}_0}{dt} &= -\tilde{x}_0 + (1 - \tilde{x}_3)Dae^{-F/\tilde{y}^2}, \\ \frac{d\tilde{x}_1}{dt} &= -\tilde{x}_1 + \tilde{y}\tilde{x}_0, \\ \frac{d\tilde{x}_2}{dt} &= -\tilde{x}_2 + \tilde{y}\tilde{x}_1, \\ \frac{d\tilde{x}_3}{dt} &= -\tilde{x}_3 + \tilde{y}\tilde{x}_2, \\ \frac{d\tilde{y}}{dt} &= \frac{1 - \tilde{y} - (\alpha - \tilde{y})\tilde{y}\tilde{x}_2}{1 - \tilde{x}_3}. \end{aligned} \quad (2.14)$$

The ability of the above fifth-order moment model to reproduce the dynamics, and to some extent the solutions, of the distributed parameter model of (2.1) is shown in Fig. 2.5, where the profiles of the total particle concentration generated by the two models are compared (both models start from the same initial conditions). Even though the discrepancy of the total particle concentration profiles predicted by the two models increases with time (this is expected due to the open-loop instability of the process), it is clear that the fifth-order moment model of (2.14) provides a very good approximation of the distributed parameter model of (2.1), thereby establishing that the dominant dynamics of the system of (2.1) are low dimensional and motivating the use of the moment model for nonlinear controller design.

For the batch crystallization process, the following low-order model can be derived from (2.3) using the method of moments:

$$\begin{aligned} \frac{d\mu_0}{dt} &= \left(1 - \frac{4}{3}\pi\mu_3\right)k_2e^{-\frac{k_3}{(c/c_s-1)^2}}e^{-\frac{E_b}{RT}}, \\ \frac{d\mu_1}{dt} &= k_1(c - c_s)e^{-\frac{E_g}{RT}}\mu_0, \\ \frac{d\mu_2}{dt} &= 2k_1(c - c_s)e^{-\frac{E_g}{RT}}\mu_1, \end{aligned}$$

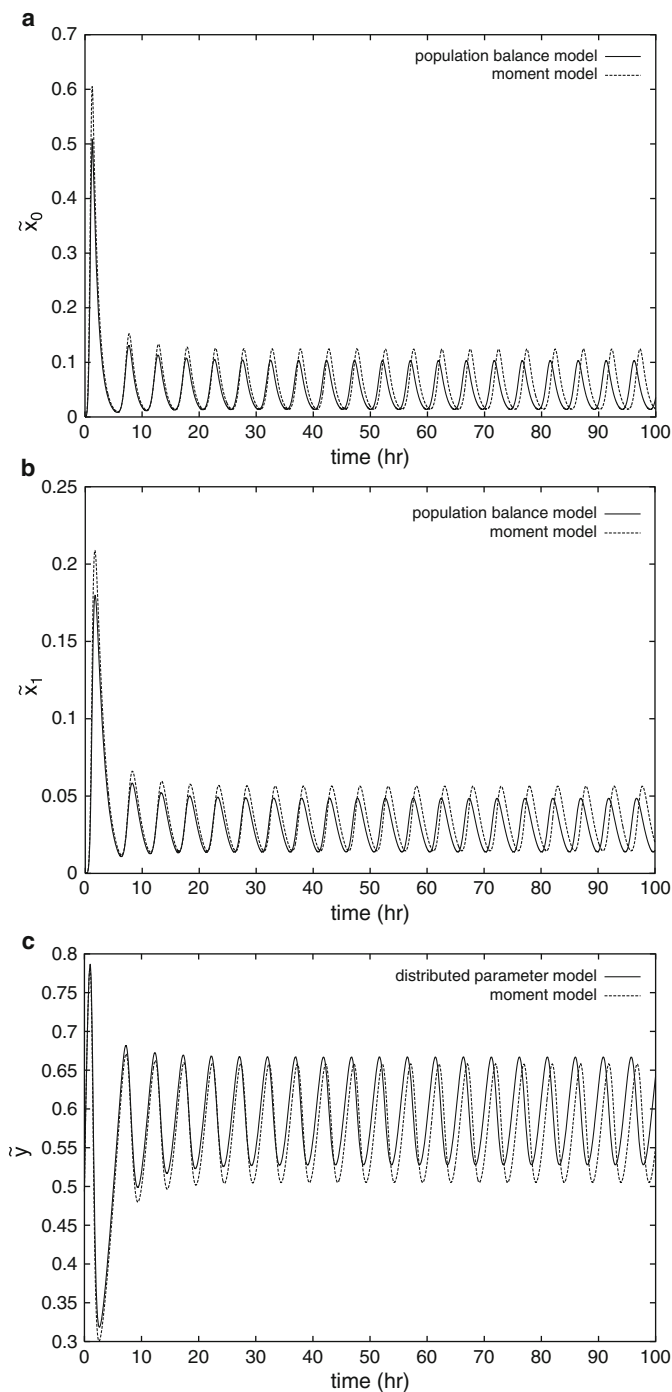


**Fig. 2.5** Comparison of open-loop profiles of (a) crystal concentration, (b) total crystal size, and (c) solute concentration obtained from the distributed parameter model and the moment model

$$\begin{aligned}
\frac{d\mu_3}{dt} &= 3k_1(c - c_s)e^{-\frac{E_g}{RT}}\mu_2, \\
\frac{dc}{dt} &= \frac{-4\pi(c - c_s)\mu_2(\rho - c)}{(1 - \frac{4}{3}\pi\mu_3)}, \\
\frac{dT}{dt} &= -\frac{\rho_c\Delta H_c}{\rho C_p}4\pi k_1(c - c_s)e^{-\frac{E_g}{RT}}\mu_2 - \frac{UA_c}{\rho C_p V}(T - T_c), \quad (2.15)
\end{aligned}$$

where  $E_g$  and  $E_b$  denote the activation energies for growth and nucleation, respectively. The objective is to control the interplay between the particle nucleation and growth rates such that a CSD with a larger average particle size is obtained at the end of the batch run by manipulating the cooling water temperature.

Based on the low-order models, nonlinear finite-dimensional state and output feedback controllers have been synthesized that guarantee stability and enforce output tracking in the closed-loop finite dimensional system. It has also been established that these controllers exponentially stabilize the closed-loop particulate process model. The output feedback controller is constructed through a standard combination of the state feedback controller with a state observer. Specifically, in the case of the continuous crystallization example, the nonlinear output feedback controller has the following form:

$$\begin{aligned}
\frac{d\omega_0}{dt} &= -\omega_0 + (1 - \omega_3)Da e^{-F/\omega_4^2} + L_0(\tilde{h}(\tilde{x}) - \tilde{h}(\omega)), \\
\frac{d\omega_1}{dt} &= -\omega_1 + \omega_4\omega_0 + L_1(\tilde{h}(\tilde{x}) - \tilde{h}(\omega)), \\
\frac{d\omega_2}{dt} &= -\omega_2 + \omega_4\omega_1 + L_2(\tilde{h}(\tilde{x}) - \tilde{h}(\omega)), \\
\frac{d\omega_3}{dt} &= -\omega_3 + \omega_4\omega_2 + L_3(\tilde{h}(\tilde{x}) - \tilde{h}(\omega)), \\
\frac{d\omega_4}{dt} &= \frac{1 - \omega_4 - (\alpha - \omega_4)\omega_4\omega_2}{1 - \omega_3} + L_4(\tilde{h}(\tilde{x}) - \tilde{h}(\omega)) \\
&\quad + \frac{[\beta_2 L_{\tilde{g}} L_{\tilde{f}} \tilde{h}(\omega)]^{-1} \left\{ v - \beta_0 \tilde{h}(\omega) - \beta_1 L_{\tilde{f}} \tilde{h}(\omega) - \beta_2 L_{\tilde{f}}^2 \tilde{h}(\omega) \right\}}{1 - \omega_3}, \\
\bar{u}(t) &= [\beta_2 L_{\tilde{g}} L_{\tilde{f}} \tilde{h}(\omega)]^{-1} \left\{ v - \beta_0 \tilde{h}(\omega) - \beta_1 L_{\tilde{f}} \tilde{h}(\omega) - \beta_2 L_{\tilde{f}}^2 \tilde{h}(\omega) \right\}, \quad (2.16)
\end{aligned}$$

where  $v$  is the set-point,  $\beta_0$ ,  $\beta_1$ ,  $\beta_2$  and  $L = [L_0 \ L_1 \ L_2 \ L_3 \ L_4]^T$  are controller parameters and  $\tilde{h}(\omega) = \omega_0$  or  $\tilde{h}(\omega) = \omega_1$ .

The nonlinear controller of (2.16) was also combined with a PI controller (that is, the term  $v - \beta_0 \tilde{h}(\omega)$  was substituted by  $v - \beta_0 \tilde{h}(\tilde{x}) + \frac{1}{\tau_i'} \xi$ , where  $\xi = v - \tilde{h}(\tilde{x})$ ,  $\xi(0) = 0$  and  $\tau_i'$  is the integral time constant) to ensure offsetless tracking in the presence of constant uncertainty in process parameters. The practical implementation of

the nonlinear controller of (2.16) requires online measurements of the controlled outputs  $\tilde{x}_0$  or  $\tilde{x}_1$ ; in practice, such measurements can be obtained by using, for example, light scattering [3, 55]. In (2.16), the feedback controller is synthesized via geometric control methods and the state observer is an extended Luenberger-type observer [6].

Several simulations have been performed in the context of the continuous crystallizer process model presented before to evaluate the performance and robustness properties of the nonlinear controllers designed based on the reduced order models, and to compare them with the ones of a PI controller. In all the simulation runs, the initial condition:

$$n(r, 0) = 0.0, c(0) = 990.0 \text{ kg/m}^3$$

was used for the process model of (2.1) and (2.2) and the finite difference method with 1,000 discretization points was used for its simulation. The crystal concentration,  $\tilde{x}_0$ , was considered to be the controlled output and the inlet solute concentration was chosen to be the manipulated input. Initially, the set-point tracking capability of the nonlinear controller was evaluated under nominal conditions for a 0.5 increase in the value of the set-point.

Figure 2.6 shows the closed-loop output (left plot) and manipulated input (right plot) profiles obtained by using the nonlinear controller (solid lines). For the sake of comparison, the corresponding profiles under proportional-integral (PI) control are also included (dashed lines); the PI controller was tuned so that the closed-loop output response exhibits the same level of overshoot to the one of the closed-loop output under non-linear control. Clearly, the nonlinear controller drives the controlled output to its new set-point value in a significantly shorter time than the one required by the PI controller, while both controlled outputs exhibit very similar overshoot. For the same simulation run, the evolution of the closed-loop profile and the final steady-state profile of the CSD are shown in Fig. 2.7. An exponentially decaying CSD is obtained at the steady state. The reader may refer to [6] for extensive simulation results.

#### 2.2.4.2 Hybrid Predictive Control

In addition to handling nonlinear behavior, an important control problem is to stabilize the crystallizer at an unstable steady-state (which corresponds to a desired PSD) using constrained control action. Currently, the achievement of high performance, under control and state constraints, relies to a large extent on the use of model predictive control (MPC) policies. In this approach, a model of the process is used to make predictions of the future process evolution and compute control actions, through repeated solution of constrained optimization problems, which ensure that the process state variables satisfy the imposed limitations. However, the ability of the available model predictive controllers to guarantee closed-loop stability and enforce constraint satisfaction is dependent on the assumption of

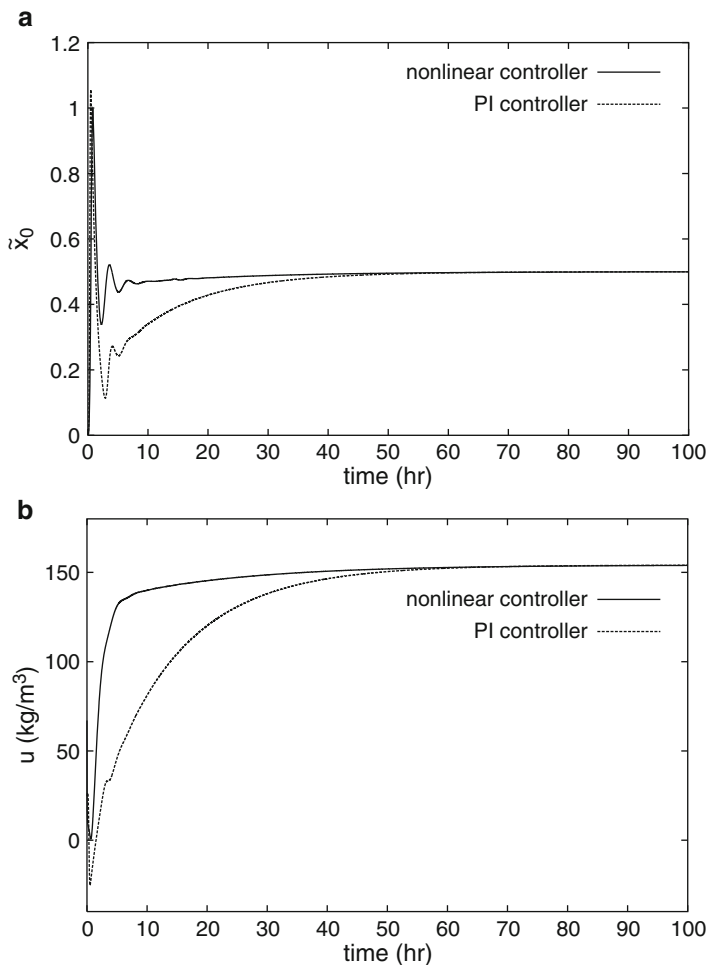


**Fig. 2.6** (a) Closed-loop output and (b) manipulated input profiles under nonlinear and PI control, for a 0.5 increase in the set-point ( $\tilde{x}_0$  is the controlled output) [6]

feasibility (i.e., existence of a solution) of the constrained optimization problem. This limitation strongly impacts the practical implementation of the MPC policies and limits the a priori (i.e., before controller implementation) characterization of the set of initial conditions starting from where the constrained optimization problem is feasible and closed-loop stability is guaranteed. This problem typically results in the need for extensive closed-loop simulations and software verification (before online implementation) to search over the whole set of possible initial operating conditions that guarantee stability. This in turn can lead to prolonged periods for plant commissioning. Alternatively, the lack of a priori knowledge of the stabilizing initial conditions may necessitate limiting process operation within a

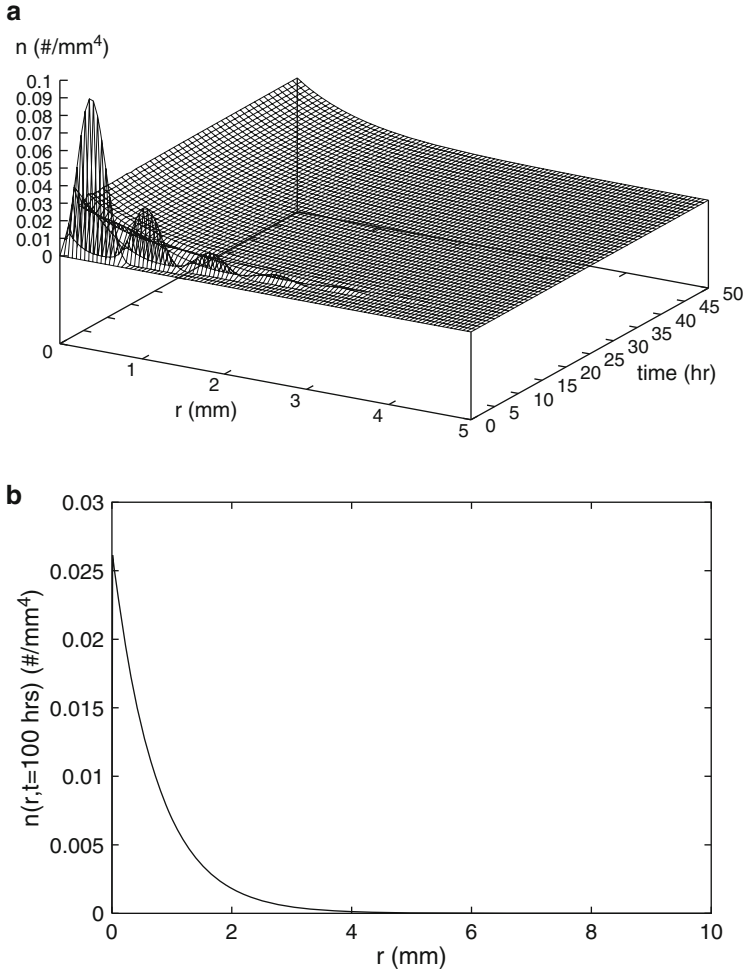


**Fig. 2.7** Profile of evolution of crystal size distribution (*top*) and final steady-state crystal size distribution (*bottom*) under nonlinear control ( $\bar{x}_0$  is the controlled output) [6]

small conservative neighborhood of the desired set-point in order to avoid extensive testing and simulations. Given the tight product quality specifications, however, both of these two remedies can impact negatively on the efficiency and profitability of the process by limiting its operational flexibility. Lyapunov-based analytical control designs allow for an explicit characterization of the constrained stability region [17, 18, 47]; however, their closed-loop performance properties cannot be transparently characterized.

To overcome these difficulties, we recently developed [20] a hybrid predictive control structure that provides a safety net for the implementation of predictive control algorithms. The central idea is to embed the implementation of MPC within



the stability region of a bounded controller and devise a set of switching rules that orchestrate the transition from MPC to the bounded controller in the event that MPC is unable to achieve closed-loop stability (e.g., due to inappropriate choice of the horizon length, infeasibility, or computational difficulties). Switching between the two controllers allows reconciling the tasks of optimal stabilization of the constrained closed-loop system (through MPC) with that of computing a priori the set of initial conditions for which closed-loop stability is guaranteed (through Lyapunov-based [17, 18] bounded nonlinear control).

We demonstrated the application of the hybrid predictive control strategy to the continuous crystallizer of (2.1) and (2.2). The control objective was to suppress the oscillatory behavior of the crystallizer and stabilize it at an unstable steady state that corresponds to a desired PSD by manipulating the inlet solute concentration. To achieve this objective, measurements or estimates of the first four moments and of the solute concentration are assumed to be available. Subsequently, the proposed methodology was employed for the design of the controllers using a low-order model constructed by using the method of moments. We compared the hybrid predictive control scheme, with an MPC controller designed with a set of stabilizing constraints and a Lyapunov-based nonlinear controller.

In the first set of simulation runs, we tested the ability of the MPC controller with the stability constraints to stabilize the crystallizer starting from the initial condition  $x(0) = [0.066 \ 0.041 \ 0.025 \ 0.015 \ 0.560]'$ , corresponding to the dimensionless moments of the CSD as well as the dimensionless concentration of the solute in the crystallizer [60]. The result is shown by the solid lines in Fig. 2.8a–e where it is seen that the predictive controller, with a horizon length of  $T = 0.25$ , is able to stabilize the closed-loop system at the desired equilibrium point. Starting from the initial condition  $x(0) = [0.033 \ 0.020 \ 0.013 \ 0.0075 \ 0.570]'$ , however, the MPC controller with the stability constraints yields no feasible solution. If the stability constraints are relaxed to make the MPC feasible, we see from the dashed lines in Fig. 2.8a–e that the resulting control action cannot stabilize the closed-loop system, and leads to a stable limit cycle. On the other hand, the bounded controller is able to stabilize the system from both initial conditions (this was guaranteed because both initial conditions lied inside the stability region of the controller). The state trajectory starting from  $x(0) = [0.033 \ 0.020 \ 0.013 \ 0.0075 \ 0.570]'$  is shown in Fig. 2.8a–e with the dotted profile. This trajectory, although stable, presents slow convergence to the equilibrium as well as a damped oscillatory behavior that the MPC does not show when it is able to stabilize the system.

When the hybrid predictive controller is implemented from the initial condition  $x(0) = [0.033 \ 0.020 \ 0.013 \ 0.0075 \ 0.570]'$ , the supervisor detects initial infeasibility of MPC and implements the bounded controller in the closed loop. As the closed-loop states evolve under the bounded controller and get closer to the desired steady state, the supervisor finds (at  $t = 5.8$  h) that the MPC becomes feasible and, therefore, implements it for all future times. Note that despite the “jump” in the control action profile as we switch from the bounded controller to MPC at  $t = 5.8$  h, (see the difference between dotted and dash-dotted profiles in Fig. 2.8f), the

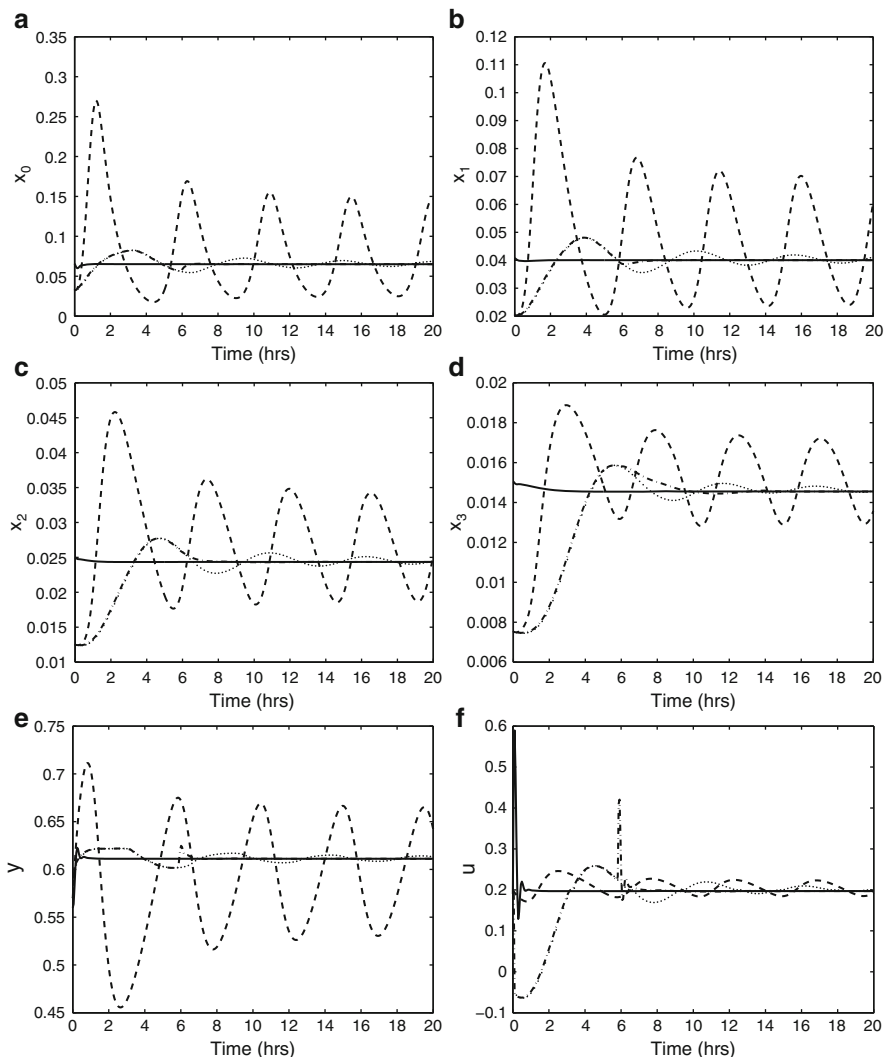


**Fig. 2.8** Continuous crystallizer example: closed-loop profiles of the dimensionless crystallizer moments (a–d), the solute concentration in the crystallizer (e) and the manipulated input (f) under MPC with stability constraints (solid lines), under MPC without stability constraints (dashed lines), under the bounded controller (dotted lines), and using the hybrid predictive controller (dash-dotted lines) [60]. Note the different initial states

moments of the PSD in the crystallizer continue to evolve smoothly (dash-dotted lines in Fig. 2.8a–e). The supervisor finds that MPC continues to be feasible and is implemented in closed-loop to stabilize the closed-loop system at the desired steady state. Compared with the simulation results under the bounded controller, the hybrid predictive controller (dash-dotted lines) stabilizes the system much faster,

and achieves a better performance, reflected in a lower value of the performance index (0.1282 vs 0.1308). The manipulated input profiles for the three scenarios are shown in Fig. 2.8f.

### 2.2.4.3 Predictive Control of Size Distribution in a Batch Protein Crystallizer

In batch crystallization, the main objective is to achieve a desired particle size distribution at the end of the batch and to satisfy state and control constraints during the whole batch run. Significant previous work has focused on CSD control in batch crystallizers, e.g., [55, 70]. In [52], a method was developed for assessing parameter uncertainty and studied its effects on the open-loop optimal control strategy, which maximized the weight mean size of the product. To improve the product quality expressed in terms of the mean size and the width of the distribution, an online optimal control methodology was developed for a seeded batch cooling crystallizer [72]. In these previous works, most efforts were focused on the open-loop optimal control of the batch crystallizer, i.e., the optimal operating condition was calculated offline based on mathematical models. The successful application of such a control strategy relies, to a large extent, on the accuracy of the models. Furthermore, an open-loop control strategy may not be able to manipulate the system to follow the optimal trajectory because of the ubiquitous existence of modeling error. Motivated by this, we developed a predictive feedback control system to maximize the volume-averaged tetragonal lysozyme crystal size (i.e.,  $\mu_4/\mu_3$  where  $\mu_3, \mu_4$  are the third and fourth moments of the CSD; see (2.11)) by manipulating the jacket temperature,  $T_j$  [60]. The principle moments are calculated from the online measured CSD,  $n$ , which can be obtained by measurement techniques such as the laser light scattering method. The concentration and crystallizer temperature are also assumed to be measured in real time. In the closed-loop control structure, a reduced-order moments model was used within the predictive controller for the purpose of prediction. The main idea is to use this model to obtain a prediction of the state of the process at the end of the batch operation,  $t_f$ , from the current measurement at time  $t$ . Using this prediction, a cost function that depends on this value is minimized subject to a set of operating constraints. Manipulation input limitations and constraints on supersaturation and crystallizer temperature are incorporated as input and state constraints on the optimization problem. The optimization algorithm computes the profile of the manipulated input  $T_j$  from the current time until the end of the batch operation interval, then the current value of the computed input is implemented on the process, and the optimization problem is resolved and the input is updated each time a new measurement is available (receding horizon control strategy). The optimization problem that is solved at each sampling instant takes the following form:

$$\begin{aligned} \min_{T_j} \quad & -\frac{\mu_4(t_f)}{\mu_3(t_f)} \\ \text{such that} \quad & \frac{d\mu_0}{dt} = k_a C \exp\left(-\frac{k_b}{\sigma^2}\right), \end{aligned}$$

$$\begin{aligned}
\frac{d\mu_i}{dt} &= ik_g \sigma^g \mu_{i-1}(t), \quad i = 1, \dots, 4, \\
\frac{dC}{dt} &= -24\rho k_v k_g \sigma^g \mu_2(t), \\
\frac{dT}{dt} &= -\frac{UA}{MC_p}(T - T_j), \\
T_{\min} &\leq T \leq T_{\max}, \\
T_{j \min} &\leq T_j \leq T_{j \max}, \\
\sigma_{\min} &\leq \sigma \leq \sigma_{\max}, \\
\left\| \frac{dC_s}{dt} \right\| &\leq k_1,
\end{aligned} \tag{2.17}$$

$$n(0, t) \leq n_{\text{fine}}, \forall t \geq t_f/2, \tag{2.18}$$

where  $T_{\min}$  and  $T_{\max}$  are the constraints on the crystallizer temperature,  $T$ , and are specified as 4°C and 22°C, respectively.  $T_{j \min}$  and  $T_{j \max}$  are the constraints on the manipulated variable,  $T_j$ , and are specified as 3°C and 22°C, respectively. The constraints on the supersaturation  $\sigma$  are  $\sigma_{\min} = 1.73$  and  $\sigma_{\max} = 2.89$ . The constant,  $k_1$ , (chosen to be 0.065mg/ml.min) specifies the maximum rate of change of the saturation concentration  $C_s$ .  $n_{\text{fine}}$  is the largest allowable number of nuclei at any time instant during the second half of the batch run, and is set to 5/ $\mu$  m/ml. In the simulation, the sampling time is 5 min, while the batch process time  $t_f$  is 24 h. The optimization problem is solved using sequential quadratic programming (SQP). A second-order accurate finite difference scheme with 3,000 discretization points is used to obtain the solution of the population balance model of (2.3). Referring to the predictive control formulation of (2.17) and (2.18), it is important to note that previous work has shown that the objective of maximizing the volume-averaged crystal size can result in a large number of fines (crystals whose size is very small compared to the mean crystal size) in the final product [49]. To enhance the ability of the predictive control strategy to maximize the performance objective while avoiding the formation of a large number of fines in the final product, the predictive controller of (2.17) and (2.18) includes a constraint (2.18) on the number of fines present in the final product. Specifically, the constraint of (2.18), by restricting the number of nuclei formed at any time instant during the second half of the batch run limits the fines in the final product. Note that predictive control without a constraint on fines can result in a product with a large number of fines (see Fig. 2.9a), which is undesirable. The implementation of the predictive controller with the constraint of (2.18), designed to reduce the fines in the product, results in a product with much less fines while still maximizing the volume-averaged crystal size (see Fig. 2.9b). The reader may refer to [60,62] for further results on the performance of the predictive controller and comparisons with the performance of two other open-loop control strategies, Constant Temperature Control (CTC) and Constant Supersaturation Control (CSC).

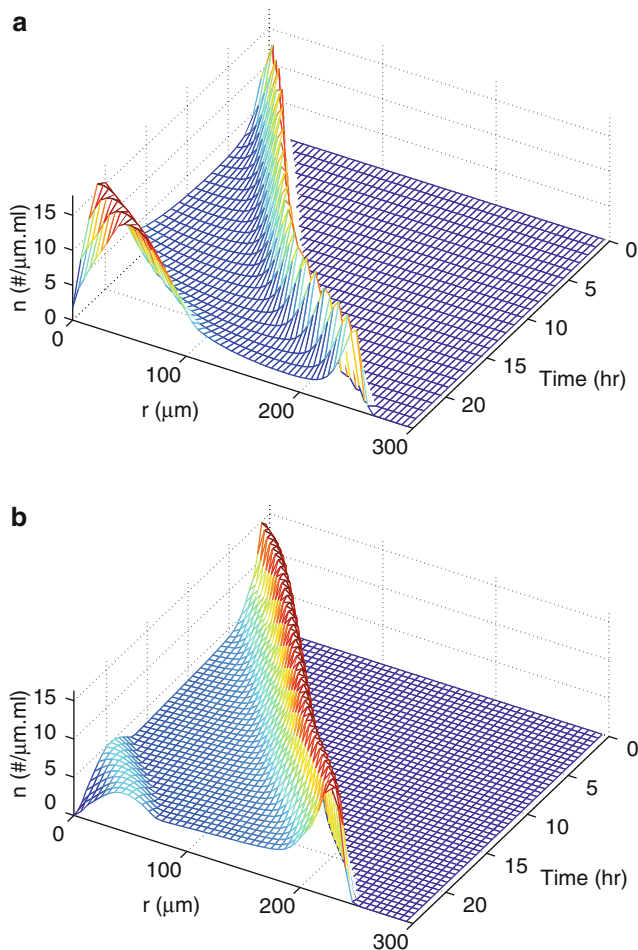


**Fig. 2.9** Evolution of particle size distribution under (a) predictive control without a constraint on fines, and (b) predictive control with a constraint on fines [62]

#### 2.2.4.4 Fault-Tolerant Control of Particulate Processes

Compared with the significant and growing body of research work on feedback control of particulate processes, the problem of designing fault-tolerant control systems for particulate processes has not received much attention. This is an important problem given the vulnerability of automatic control systems to faults (e.g., malfunctions in the control actuators, measurement sensors, or process equipment), and the detrimental effects that such faults can have on the process operating efficiency and product quality. Given that particulate processes play a key role in a wide range of industries (e.g., chemical, food, and pharmaceutical)

where the ability to consistently meet stringent product specifications is critical to the product utility, it is imperative that systematic methods for the timely diagnosis and handling of faults be developed to minimize production losses that could result from operational failures. Motivated by these considerations, recent research efforts have started to tackle this problem by bringing together tools from model-based control, infinite-dimensional systems, fault diagnosis, and hybrid systems theory. For particulate processes modeled by population balance equations with control constraints, actuator faults, and a limited number of process measurements, a fault-tolerant control architecture that integrates model-based fault detection, feedback and supervisory control has recently been developed in [19]. The architecture, which is based on reduced-order models that capture the dominant dynamics of the particulate process, consists of a family of control configurations, together with a fault detection filter and a supervisor. For each configuration, a stabilizing output feedback controller with well-characterized stability properties is designed through a combination of a state feedback controller and a state observer that uses the available measurements of the principal moments of the PSD and the continuous-phase variables to provide appropriate state estimates. A fault detection filter that simulates the behavior of the fault-free, reduced-order model is then designed, and its discrepancy from the behavior of the actual process state estimates is used as a residual for fault detection. Finally, a switching law based on the stability regions of the constituent control configurations is derived to reconfigure the control system in a way that preserves closed-loop stability in the event of fault detection. Appropriate fault detection thresholds and control reconfiguration criteria that account for model reduction and state estimation errors were derived for the implementation of the control architecture on the particulate process. The methodology was successfully applied to a continuous crystallizer example using computer simulations where the control objective was to stabilize an unstable steady state and achieve a desired CSD in the presence of constraints and actuator faults.

In addition to the synthesis of actuator fault-tolerant control systems for particulate processes, recent research efforts have also investigated the problem of preserving closed-loop stability and performance of particulate processes in the presence of sensor data losses [24]. Typical sources of sensor data losses include measurement sampling losses, intermittent failures associated with measurement techniques, as well as data packet losses over transmission lines. In this work, two representative particulate process examples – a continuous crystallizer and a batch protein crystallizer – were considered. In both examples, feedback control systems were first designed on the basis of low-order models and applied to the population balance models to enforce closed-loop stability and constraint satisfaction. Subsequently, the robustness of the control systems in the presence of sensor data losses was investigated using a stochastic formulation developed in [51] that models sensor failures as a random Poisson process. In the case of the continuous crystallizer, a Lyapunov-based nonlinear output feedback controller was designed and shown to stabilize an open-loop unstable steady state of the population balance model in the presence of input constraints. Analysis of the closed-loop system under sensor malfunctions showed that the controller is robust

with respect to significant sensor data losses, but cannot maintain closed-loop stability when the rate of data losses exceeds a certain threshold. In the case of the batch crystallizer, a predictive controller was designed to obtain a desired CSD at the end of the batch while satisfying state and input constraints. Simulation results showed how constraint modification in the predictive controller formulation can assist in achieving constraint satisfaction under sensor data losses.

#### 2.2.4.5 Nonlinear Control of Aerosol Reactors

The crystallization process examples discussed in the previous section share the common characteristic of having two independent variables (time and particle size). In such a case, order reduction, for example with the method of moments, leads to a set of ODEs in time as a reduced-order model. This is not the case, however, when three or more independent variables (time, particle size, and space) are used in the process model. An example of such a process is the aerosol flow reactor presented in the Introduction section. The complexity of the partial integro-differential equation model of (2.6) does not allow its direct use for the synthesis of a practically implementable nonlinear model-based feedback controller for spatially inhomogeneous aerosol processes. Therefore, we developed [33–35] a model-based controller design method for spatially inhomogeneous aerosol processes, which is based on the experimental observation that many aerosol size distributions can be adequately approximated by lognormal functions. The proposed control method can be summarized as follows:

1. Initially, the aerosol size distribution is assumed to be described by a lognormal function and the method of moments is applied to the aerosol population balance model of (2.6) to compute a hyperbolic partial differential equation (PDE) system (where the independent variables are time and space) that describes the spatiotemporal behavior of the three leading moments needed to exactly describe the evolution of the lognormal aerosol size distribution.
2. Then nonlinear geometric control methods for hyperbolic PDEs [10] are applied to the resulting system to synthesize nonlinear distributed output feedback controllers that use process measurements at different locations along the length of the process to adjust the manipulated input (typically, wall temperature), in order to achieve an aerosol size distribution with desired characteristics (e.g., geometric average particle volume).

We carried out an application of this nonlinear control method to an aerosol flow reactor, including nucleation, condensation, and coagulation, used to produce  $\text{NH}_4\text{Cl}$  particles [33] and a titania aerosol reactor [34]. Specifically, for an aerosol flow reactor used to produce  $\text{NH}_4\text{Cl}$  particles, the following chemical reaction takes place  $\text{NH}_3 + \text{HCl} \rightarrow \text{NH}_4\text{Cl}$  where  $\text{NH}_3$ ,  $\text{HCl}$  are the reactant species and  $\text{NH}_4\text{Cl}$  is the monomer product species. Under the assumption of lognormal aerosol size distribution, the mathematical model that describes the evolution of the first three

moments of the distribution, together with the monomer ( $\text{NH}_4\text{Cl}$ ) and reactant ( $\text{NH}_3$ ,  $\text{HCl}$ ) concentrations and reactor temperature takes the form:

$$\begin{aligned}
 \frac{\partial N}{\partial \theta} &= -v_{zl} \frac{\partial N}{\partial \bar{z}} + I' - \xi N^2, \\
 \frac{\partial V}{\partial \theta} &= -v_{zl} \frac{\partial V}{\partial \bar{z}} + I'k^* + \eta(S-1)N, \\
 \frac{\partial V_2}{\partial \theta} &= -v_{zl} \frac{\partial V_2}{\partial \bar{z}} + I'k^{*2} + 2\varepsilon(S-1)V + 2\xi V^2, \\
 \frac{\partial S}{\partial \theta} &= -v_{zl} \frac{\partial S}{\partial \bar{z}} + C\bar{C}_1\bar{C}_2 - I'k^* - \eta(S-1)N, \\
 \frac{\partial \bar{C}_1}{\partial \theta} &= -v_{zl} \frac{\partial \bar{C}_1}{\partial \bar{z}} - A_1\bar{C}_1\bar{C}_2, \\
 \frac{\partial \bar{C}_2}{\partial \theta} &= -v_{zl} \frac{\partial \bar{C}_2}{\partial \bar{z}} - A_2\bar{C}_1\bar{C}_2, \\
 \frac{\partial \bar{T}}{\partial \theta} &= -v_{zl} \frac{\partial \bar{T}}{\partial \bar{z}} + B\bar{C}_1\bar{C}_2\bar{T} + E\bar{T}(\bar{T}_w - \bar{T}),
 \end{aligned} \tag{2.19}$$

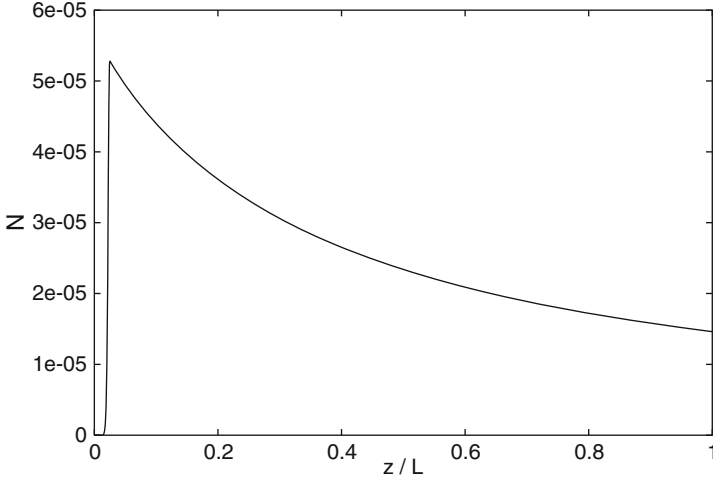
where  $\theta$  is the dimensionless time,  $\bar{z}$  is the dimensionless length,  $v_{zl}$  is the dimensionless velocity,  $I'$  is the dimensionless nucleation rate,  $S$  is the saturation ratio,  $\bar{C}_1$  and  $\bar{C}_2$  are the dimensionless concentrations of  $\text{NH}_3$  and  $\text{HCl}$ , respectively,  $\bar{T}$ ,  $\bar{T}_w$  are the dimensionless reactor and wall temperatures, respectively, and  $A_1, A_2, B, C, E$  are dimensionless quantities [33]. The controlled output is the geometric average particle volume in the outlet of the reactor, and the manipulated input is the wall temperature.

Figure 2.10 displays the steady-state profile of the dimensionless total particle concentration,  $N$ , as a function of reactor length. As expected,  $N$  increases very fast close to the inlet of the reactor (approximately, the first 3% of the reactor) due to a nucleation burst, and then, it slowly decreases in the remaining part of the reactor due to coagulation. Even though coagulation decreases the total number of particles, it leads to the formation of bigger particles, and thus, it increases the geometric average particle volume,  $v_g$ . We formulate the control problem as the one of controlling the geometric average particle volume in the outlet of the reactor,  $v_g(1, \theta)$ , ( $v_g(1, \theta)$  is directly related to the geometric average particle diameter, and hence, it is a key product characteristic of industrial aerosol processes) by manipulating the wall temperature, i.e.:

$$y(\theta) = \mathcal{C}v_g = v_g(1, \theta), \quad u(\theta) = \bar{T}_w(\theta) - \bar{T}_{ws}, \tag{2.20}$$

where  $\mathcal{C}(\cdot) = \int_0^1 \delta(\bar{z} - 1)(\cdot) d\bar{z}$  and  $\bar{T}_{ws} = T_{ws}/T_o = 1$ . Since coagulation is the main mechanism that determines the size of the aerosol particles, we focus on controlling the part of the reactor where coagulation occurs. Therefore, the wall temperature is





**Fig. 2.10** Steady-state profile of dimensionless particle concentration

assumed to be equal to its steady-state value in the first 3.5% of the reactor (where nucleation mainly occurs), and it is adjusted by the controller in the remaining part of the reactor (where coagulation takes place).

The model of (2.19) was used as the basis for the synthesis of a nonlinear controller utilizing the above-mentioned control method. For this model,  $\sigma$  (geometric standard deviation of particle number distribution) was found to be equal to 2 and the necessary controller was synthesized using the nonlinear distributed state feedback formula developed in [10] and is of the form:

$$u = \left[ \mathcal{C} \gamma_{\sigma} L_g \left( \sum_{j=1}^n \frac{\partial x_j}{\partial \bar{z}} L_{a_j} + L_f \right) h(x) b(\bar{z}) \right]^{-1} \left\{ y_{sp} - \mathcal{C} h(x) - \sum_{v=1}^2 \mathcal{C} \gamma_v \left( \sum_{j=1}^n \frac{\partial x_j}{\partial \bar{z}} L_{a_j} + L_f \right)^v h(x) \right\}, \quad (2.21)$$

where  $\gamma_1 = 580$  and  $\gamma_2 = 1.6 \times 10^5$  to enforce a slightly underdamped response.

Two simulation runs were performed to evaluate the set-point tracking capabilities of the nonlinear controller and compare its performance with a proportional-integral controller. In both simulation runs, the aerosol reactor was initially assumed to be at steady-state and a 5% increase in the set-point value of  $v_g(1, 0)$  was imposed at  $t = 0$  s (i.e.,  $y_{sp} = 1.05 v_g(1, 0)$ ). Figure 2.11 (top plot – solid line) shows the profile of the controlled output which is the mean particle volume at the outlet of the reactor  $v_g(1, t)$ , while Fig. 2.11 (bottom plot – solid line) displays the corresponding profile of the manipulated input which is the wall temperature. The nonlinear controller

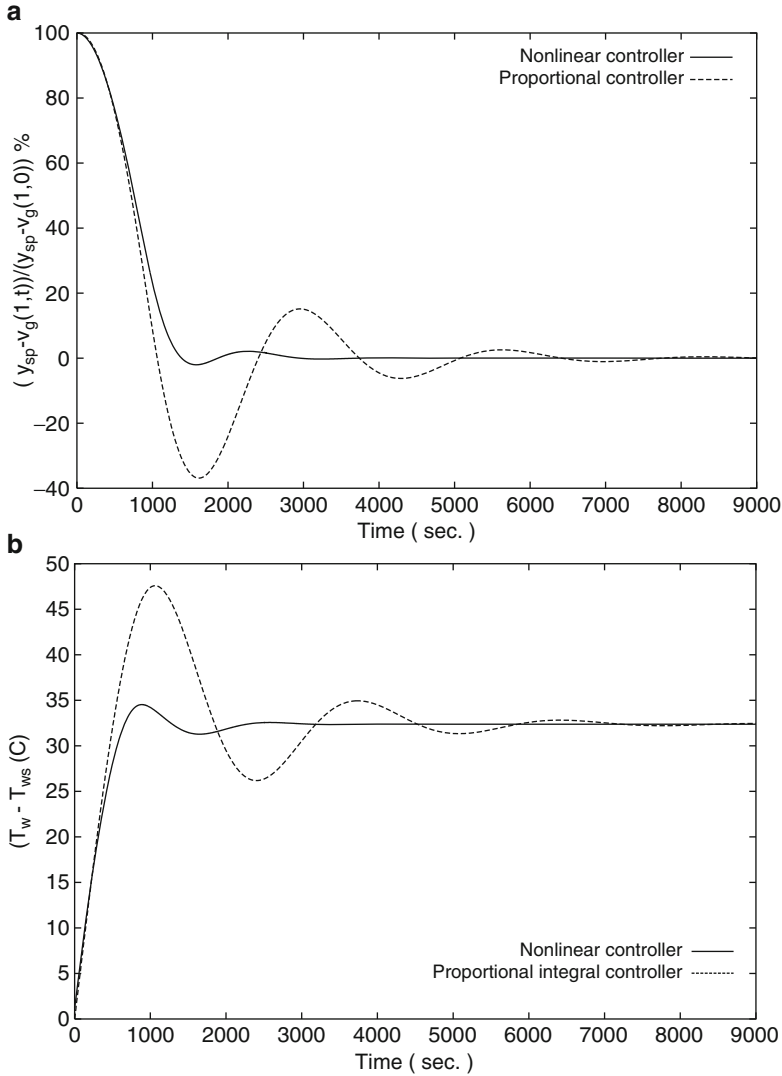


**Fig. 2.11** (a) Closed-loop profiles of scaled mean particle volume in the outlet of the reactor under proportional-integral and nonlinear controllers. (b) Manipulated input profiles for proportional-integral and nonlinear controllers [33]

of (2.21) regulates  $v_g(1, t)$  successfully to its new set-point value. For the sake of comparison, we also implemented on the process a proportional-integral controller; this controller was tuned so that the time at which the closed-loop output needs to reach the final steady state is the same as for the closed-loop output under nonlinear control. The profiles of the controlled output and manipulated input are shown in

Fig. 2.11 (dashed lines show the corresponding profiles for the proportional-integral controller). It is clear that the nonlinear controller outperforms the proportional-integral controller.

## 2.3 Multiscale Modeling and Control of HVOF Thermal Spray Coating Processes

### 2.3.1 Multiscale Modeling of Coating Microstructure

The past decade has witnessed a shift of synthesis to processing in nanotechnology research, i.e. the manufacture of functional coatings and bulk structures using nanostructured powders [5]. One example is HVOF thermal spray processing of functional coatings from nanostructured agglomerate powders. The nanostructured coatings prepared by HVOF are extensively used in many industries as thermal-barrier and wear-resistant surface layers to extend product life, increase performance, and reduce production and maintenance costs. Thermal spray has also been a molding method for the fabrication of micro-components [69].

A representative diagram of the HVOF thermal spray process is shown in Fig. 2.12. The high-pressure combustion of a fuel (typically hydrogen, propane, or kerosene) with oxygen generates a supersonic jet, which propels and heats up the powder of particles added to the gas stream. The powder particles are accelerated, softened in the gas stream, and deformed on the substrate, forming a dense coating.

Because the highly coupled transport phenomena of the HVOF thermal spray cannot be fully revealed by experimental studies, mathematical modeling has been an excellent complement in order to provide system-level understanding of the underlying physics of the HVOF thermal spray process to guide optimal system design and operation [14, 53]. Moreover, to fabricate coatings of a consistent quality, the compensation of feed disturbances and process variability during real-time process

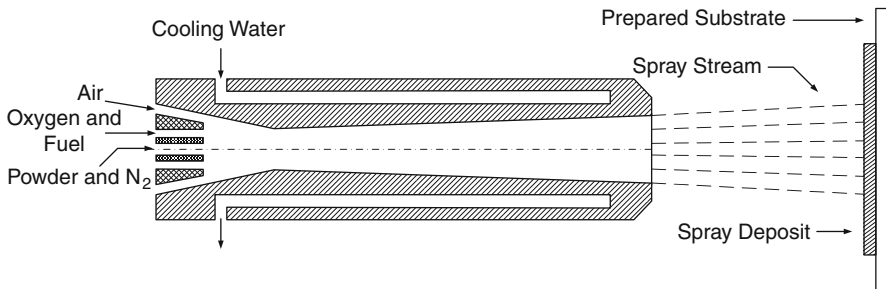
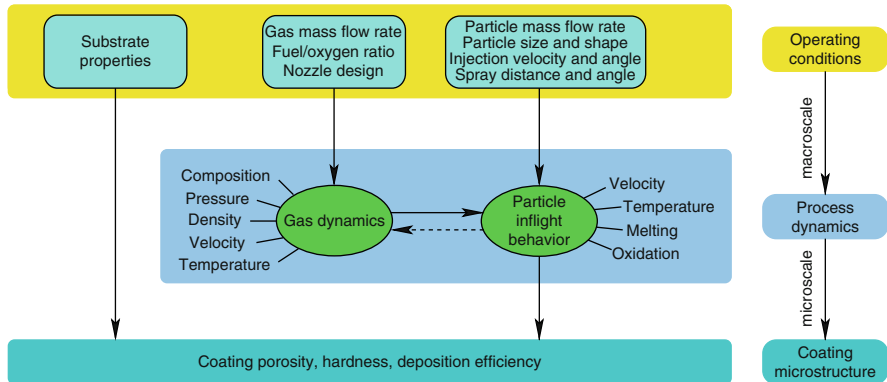


Fig. 2.12 Schematic of a representative HVOF thermal spray process



**Fig. 2.13** Multiscale character of the HVOF thermal spray process [44]

operation becomes essential. This motivates the development and implementation of real-time control systems in the HVOF thermal spray process to suppress variations in the particle characteristics at the point of impact on the substrate. The major challenge in this problem is the development of multiscale models linking the macroscopic scale process behavior (i.e., gas dynamics and particle inflight behavior) and the microscopic scale process characteristics (evolution of coating microstructure), and the integration of models, measurements, and control theory to develop measurement/model-based control strategies. The multiscale character of the HVOF thermal spray process is shown in Fig. 2.13. The microstructure of HVOF-sprayed coatings results from the deformation, solidification, and sintering of the deposited particles, which are dependent on the substrate properties (e.g., substrate temperature) as well as the physical and chemical state (e.g., temperature, velocity, melting ratio, and oxidant content) of the particles at the point of impact on the substrate. On the other hand, the particle inflight characteristics are coupled with the gas dynamics, which can be manipulated by adjusting operating conditions such as the gas flow rates of fuel and oxygen. While the macroscopic thermal/flow field can be readily described by continuum type differential equations governing the compressible two-phase flow, the process of particle deposition is stochastic and discrete in nature, and thus, it can be best described by stochastic simulation methods [36]. By manipulating macro-scale operating conditions such as gas feed flow rates, one can control the coating microstructure which determines the coating mechanical and physical properties.

In the past several years, we developed a multiscale computational framework for the HVOF thermal spray processing of nanostructured coatings [40–46, 61]. The multiscale process model encompasses gas dynamics of the supersonic reacting flow, evolution of particle velocity, temperature and molten state during flight, and stochastic growth of coating microstructure, as shown in Fig. 2.14. The modeling work demonstrates that the coating microstructure, porosity, and roughness, as well as the deposition efficiency, are highly dependent on the particle

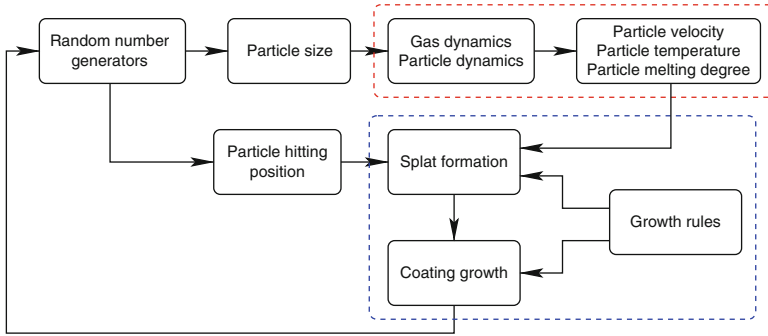


**Fig. 2.14** Multiscale modeling of the HVOF thermal spray process (based on [44, 61])

characteristics (primarily velocity, temperature, and molten state), which is consistent with experimental observations [26, 28, 29]. For example, the effect of particle melting degree on the coating microstructure is shown in Fig. 2.15 [42]. When all the particles are fully melted, which is typical in a plasma spray, an ideal lamellar microstructure is formed. However, under normal HVOF processing conditions, many particles might be partially melted or even unmelted [44, 71]. When a partially melted particle lands on the substrate and deforms, the resulting splat typically has a “fried-egg” shape which features a nearly hemispherical core located in the center of a thin disk [31]. As a result, a different coating microstructure is formed which deviates from the ideal lamellar microstructure. The fact that the particles are not necessarily fully melted to form a coating with excellent microstructure is very important in the processing of nanostructured coatings because the nanostructure in the powder particles could be destroyed if the particles are heated too much and go through a phase change during flight. However, if the particle melting degree is very low, unmelted particles may bounce off the substrate, resulting in a high-porosity coating with a low deposition efficiency. In addition to particle melting degree, the model also predicts that the higher the particle impact velocity, the higher the flattening ratio. As a result, the coating porosity is lower and the coating is denser.

### 2.3.2 Control of Particle Velocity and Temperature in HVOF Thermal Spray

Based on the above analysis, one should suppress the variation in the particle characteristics upon impact on the substrate to enhance the consistency of the coating quality. Both modeling and experimental studies [44, 65, 67] reveal that the particle velocity and temperature (or melting degree) at impact with the substrate can be almost independently adjusted by manipulating the pressure in the combustion chamber and the fuel/oxygen ratio. As shown in Fig. 2.16, when the combustion pressure increases from 5 bar to 15 bar with a fixed equivalence ratio

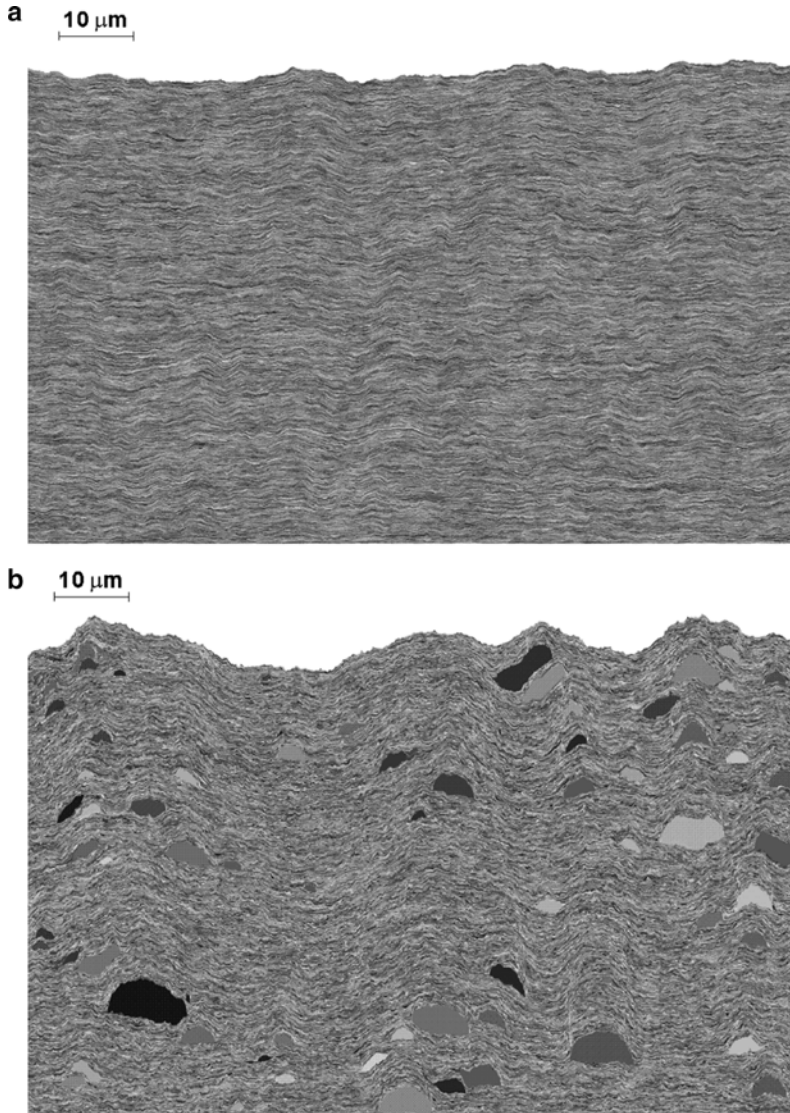


**Fig. 2.15** Simulated microstructure of coatings formed by fully melted particles and particles with mixed molten states [42]

(or the fuel/oxygen ratio divided by its stoichiometric value), the gas momentum flux ( $\rho v_g^2$ ), which is roughly proportional to the drag force for particle motion, is almost tripled. However, the gas temperature increases by about 4% only. When the equivalence ratio varies from 0.5 to 1.5 with a fixed chamber pressure, the gas temperature varies about 12% from its lowest value to the peak occurring at an equivalence ratio around 1.2. However, the gas momentum flux remains almost the

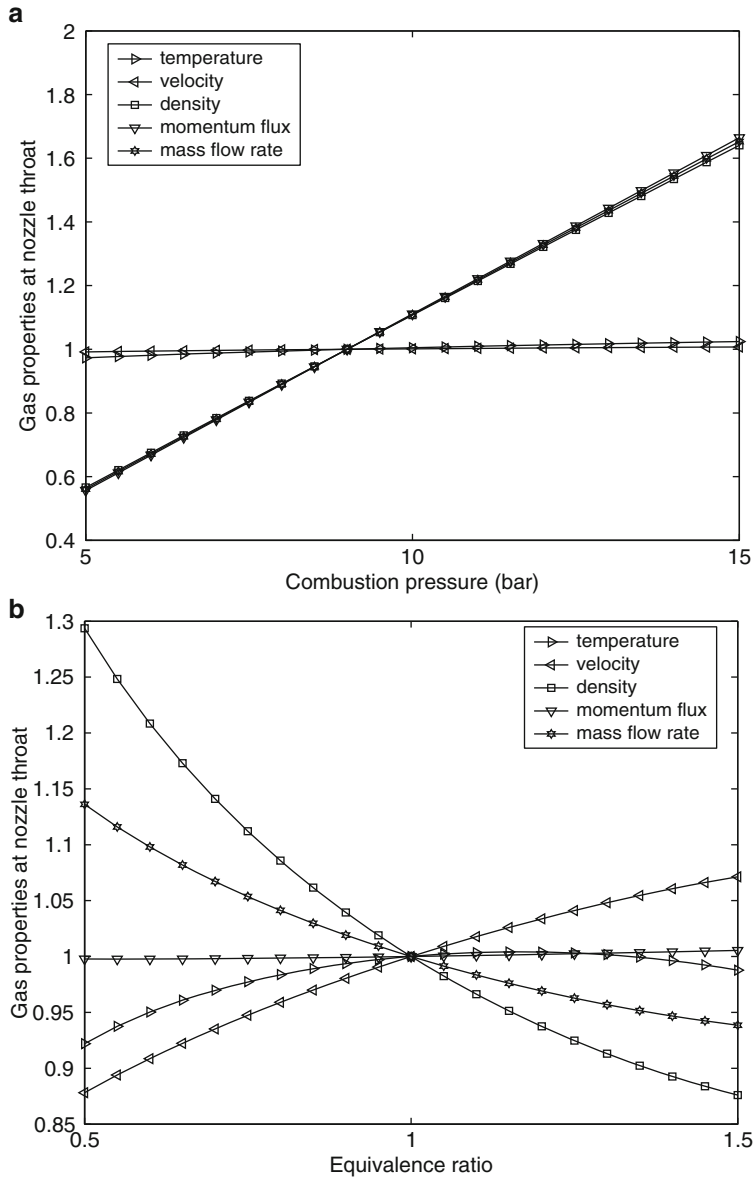


**Fig. 2.16** Influence of pressure and fuel/oxygen ratio on gas momentum flux and gas temperature [44]

same in the entire range. It is worth noting that the window for particle temperature control in the HVOF thermal spray is narrower than in the plasma spray where the particle temperature can be adjusted in a wider range by manipulating the torch current [21].

Based on the model predictions and available experimental observations, the control problem for the HVOF process is formulated as the one of regulating the volume-based averages of velocity and temperature (or melting degree) of particles at impact on the substrate by manipulating the flow rates of fuel and oxygen at the entrance of the HVOF thermal spray gun. The particle sensing including temperature, velocity, and size can be provided by a variety of online diagnostic techniques developed by different groups [22, 27, 66]. The manipulation of combustion pressure and equivalence ratio is realized by adjusting the flow rate of fuel,  $u_1(t)$ , and oxygen,  $u_2(t)$  (see (2.23) below). Note that the chamber pressure is dependent on the flow rates of fuel and oxygen as follows:

$$\dot{m} = \frac{p_0}{\sqrt{T_0}} A_{\text{th}} \sqrt{\frac{\gamma \bar{M}_{\text{pr}}}{R_g} \left( \frac{2}{\gamma + 1} \right)^{\frac{\gamma+1}{\gamma-1}}}, \quad (2.22)$$

where  $\dot{m}$  is the total mass flow rate,  $A_{\text{th}}$  is the cross-sectional area at the throat (where the area is the minimum),  $R_g$  is the molecular gas constant,  $\bar{M}_{\text{pr}}$  is the average molecular weight of the combustion products, and  $T_0$  and  $p_0$  are the stagnation temperature and stagnation pressure in the combustion chamber, respectively.

Owing to the almost decoupled nature of the manipulated input/controlled output pairs, two proportional-integral (PI) controllers were proposed in [41, 44] to regulate the process. Specifically, the controllers have the following form:

$$\begin{aligned} \dot{\zeta}_i &= y_{\text{sp}_i} - y_i, \quad \zeta_i(0) = 0, \quad i = 1, 2 \\ u'_i &= K_{c_i} \left[ (y_{\text{sp}_i} - y_i) + \frac{1}{\tau_{c_i}} \zeta_i \right] + u'_{0_i}, \quad i = 1, 2 \\ \{u_1, u_2\} &= f(u'_1, u'_2), \end{aligned} \quad (2.23)$$

where  $y_{\text{sp}_i}$  is the desired set-point value and  $y_i$  is the value of the output obtained from the measurement system ( $y_1$  is the volume-based average of particle velocity and  $y_2$  is the volume-based average of particle temperature or melting degree),  $u'_1$  is the combustion pressure and  $u'_2$  is the equivalence ratio.  $f$  is the mapping between the flow rates and the chamber pressure as well as the equivalence ratio.  $K_{c_i}$  is the proportional gain and  $\tau_{c_i}$  is the integral time constant. If the gas phase measurement is available, a model-based scheme can be used to estimate the particle properties through the dynamic particle-inflight model [45].

Closed-loop simulations under the control scheme of (2.23) have been carried out to demonstrate the effectiveness of the proposed control formulation [46]. It is assumed in the computer simulations that the responses of gas and particle dynamics to the change of gas flow rates are very fast, which is reasonable for such a supersonic flow. With this simplification, it has been demonstrated that the feedback controllers are very effective with respect to set-point changes in both particle velocity and temperature (i.e., 5% increase in both particle velocity and melting degree). As seen in Fig. 2.17, both the flow rates of oxygen and fuel increase



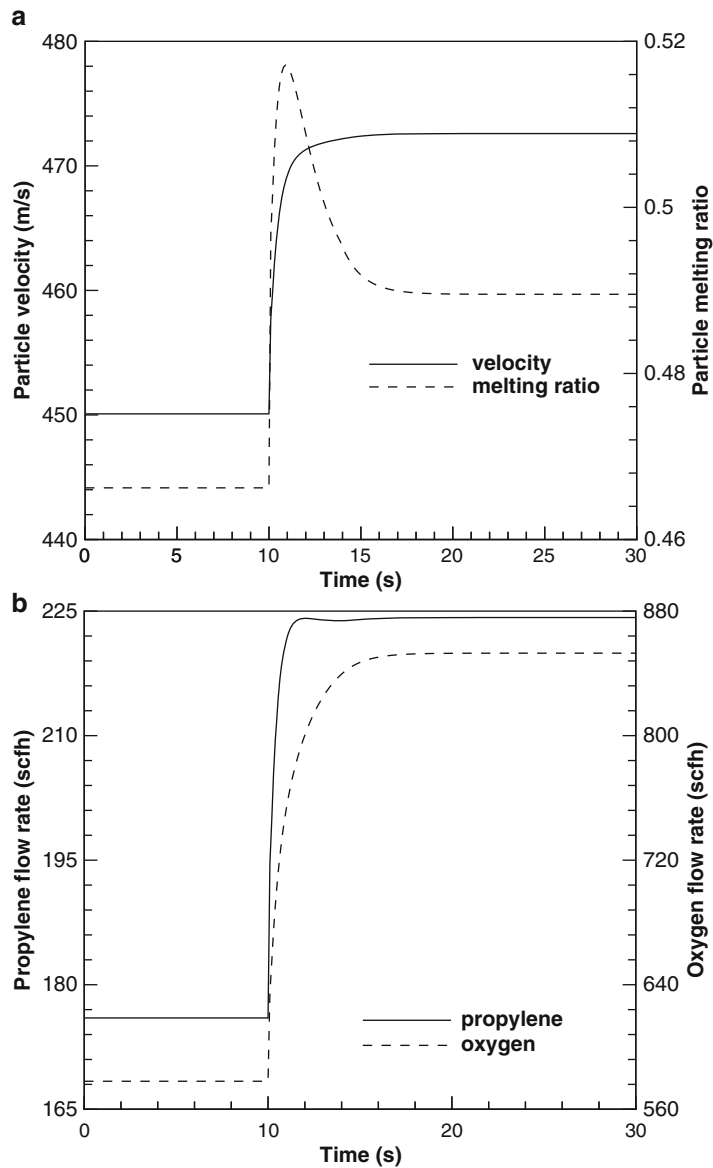


**Fig. 2.17** Profiles of (a) controlled outputs (average particle velocity and melting ratio) and (b) manipulated inputs (flow rates of propylene and oxygen) under the request of 5% increase in particle velocity and 5% increase in melting ratio [46]

in order to have a higher particle velocity. However, the temperature increases and exceeds its desired value due to the increased chamber pressure. As a result, the rate of change of oxygen flow becomes slower than the one of fuel after a short period of

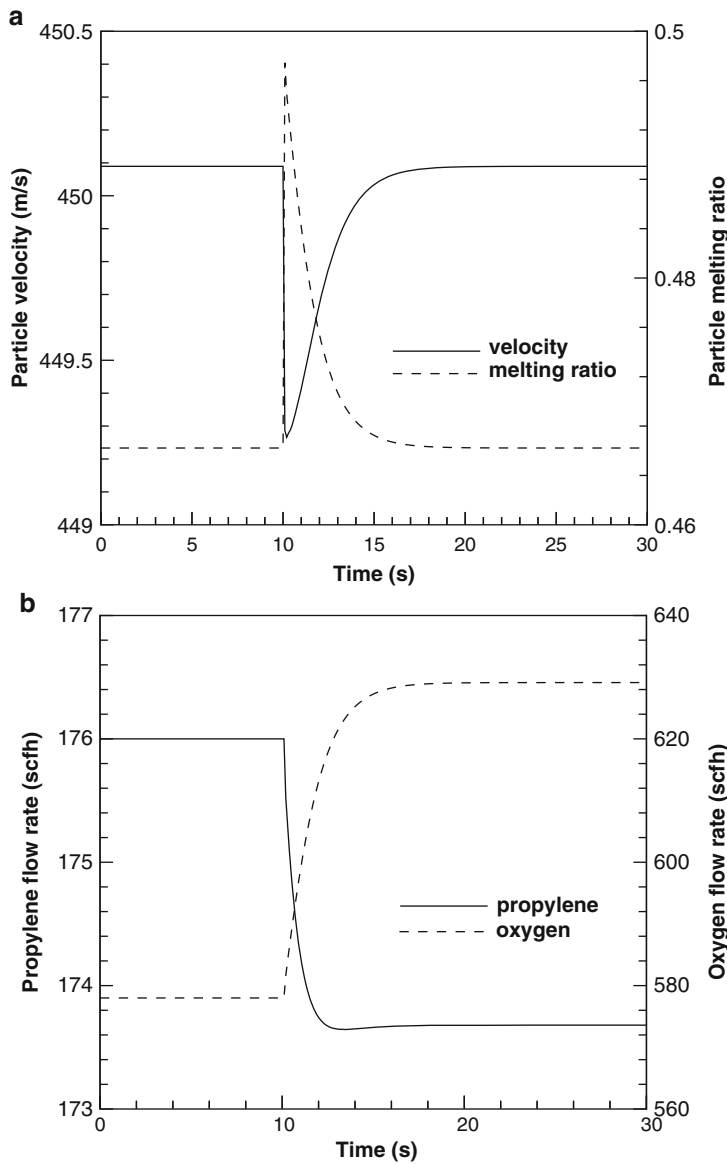


**Fig. 2.18** Profiles of (a) controlled outputs (average particle velocity and melting ratio) and (b) manipulated inputs (flow rates of propylene and oxygen) in the presence of 10% decrease in spray distance [46]

time, which lowers the equivalence ratio and drives the temperature down to its set point. Figure 2.18 demonstrates the response of the feedback controller in order to maintain the same particle velocity and temperature levels in the presence of a 10%

decrease in the spray distance (process disturbance). The particle velocity does not change much while the particle temperature increases significantly. Under feedback control, the manipulated inputs adjust to drive the process outputs to their original steady-state values in 10 s, which demonstrates the robustness of the controller.

To the best knowledge of the authors, no experimental implementation of HVOF thermal spray control has been reported. Feedback control of average particle temperature and velocity in plasma spray has been studied by Fincke et al. [21]. With the development of fast and reliable online gas and particle sensing and diagnostic tools by companies and institutions (e.g., Idaho National Laboratory, Tecnar Automation, Canada, and Oseir Ltd., Finland), the demonstration of HVOF spray control should be expected in the near future.

## 2.4 Conclusions

Control of particulate processes systems is a cross-disciplinary and rapidly growing research area that brings together fundamental modeling, numerical simulation, nonlinear dynamics, and control theory. This chapter presents recent advances in systematic methods for the design of easy-to-implement nonlinear feedback controllers for broad classes of particulate processes. It is expected that feedback control will play an important role in the synthesis and processing of nano- and micro-size particles with the ever-increasing research and development in advanced materials and semiconductor manufacturing, nanotechnology, and biotechnology. The reader may refer to [11] for a detailed discussion on future problems on control of particulate processes.

**Acknowledgements** Financial support from the NSF (ITR), CTS-0325246, and the Office of Naval Research (2001 Young Investigator Award) is gratefully acknowledged. The authors note that all the figures included in this Chapter are original and have permission to include them in the present chapter.

## References

1. L. Ajdelsztajn, F. Tang, J.M. Schoenung, G.E. Kim, and V. Provenzano. Synthesis and oxidation behavior of nanocrystalline MCrAlY bond coatings. *J. Thermal Spray Technol.*, 14:23–30, 2005.
2. A. Azarani. Automated high-throughput protein crystallization. In *The proteomics protocols handbook*, Walker, J. M. (Ed.), pages 955–966. Humana Press, Totowa, New Jersey, 2005.
3. C.F. Bohren, and D.R. Huffman. *Absorption and scattering of light by small particles*. Wiley, New York, 1983.
4. R.D. Braatz, and S. Hasebe. Particle size and shape control in crystallization processes. In *AIChE Symposium Series: Proceedings of 6th international conference on chemical process control*, Rawlings, J. B. et al. (Eds.), pages 307–327, 2002.

5. D. Cheng, G. Trapaga, J.W. McKelliget, and E.J. Lavernia. Mathematical modelling of high velocity oxygen fuel thermal spraying of nanocrystalline materials: an overview. *Modell. Simul. Mater. Sci. Eng.*, 11:R1–R31, 2003.
6. T. Chiu, and P.D. Christofides. Nonlinear control of particulate processes. *AIChE J.*, 45: 1279–1297, 1999.
7. T. Chiu, and P.D. Christofides. Robust control of particulate processes using uncertain population balances. *AIChE J.*, 46:266–280, 2000.
8. P.D. Christofides. *Model-based control of particulate processes*. Kluwer Academic Publishers, Particle Technology Series, Netherlands, 2002.
9. P.D. Christofides, and T. Chiu. Nonlinear control of particulate processes. In *AIChE annual meeting, paper 196a, Los Angeles, CA*, 1997.
10. P.D. Christofides, and P. Daoutidis. Feedback control of hyperbolic PDE systems. *AIChE J.*, 42:3063–3086, 1996.
11. P.D. Christofides, M. Li, and L. Mädler. Control of particulate processes: Recent results and future challenges. *Powder Technol.*, 175:1–7, 2007.
12. P. Daoutidis, and M. Henson. Dynamics and control of cell populations. In *Proceedings of 6th international conference on chemical process control*, pages 308–325, Tucson, AZ, 2001.
13. J. Dimitratos, G. Elicabe, and C. Georgakis. Control of emulsion polymerization reactors. *AIChE J.*, 40:1993–2021, 1994.
14. E. Dongmo, M. Wenzelburger, and R. Gadow. Analysis and optimization of the HVOF process by combined experimental and numerical approaches. *Surf. Coat. Technol.*, 202:4470–4478, 2008.
15. F.J. Doyle, M. Soroush, and C. Cordeiro. Control of product quality in polymerization processes. In *AIChE symposium series: Proceedings of 6th international conference on chemical process control*, rawlings, J. B. et al. (Eds.), pages 290–306, 2002.
16. N.H. El-Farra, T. Chiu, and P.D. Christofides. Analysis and control of particulate processes with input constraints. *AIChE J.*, 47:1849–1865, 2001.
17. N.H. El-Farra, and P.D. Christofides. Integrating robustness, optimality, and constraints in control of nonlinear processes. *Chem. Eng. Sci.*, 56:1–28, 2001.
18. N.H. El-Farra, and P.D. Christofides. Bounded robust control of constrained multivariable nonlinear processes. *Chem. Eng. Sci.*, 58:3025–3047, 2003.
19. N.H. El-Farra, and A. Giridhar. Detection and management of actuator faults in controlled particulate processes using population balance models. *Chem. Eng. Sci.*, 63:1185–1204, 2008.
20. N.H. El-Farra, P. Mhaskar, and P.D. Christofides. Hybrid predictive control of nonlinear systems: Method and applications to chemical processes. *Int. J. Robust Nonlinear Control*, 14:199–225, 2004.
21. J.R. Fincke, W.D. Swank, R.L. Bewley, D.C. Haggard, M. Gevelber, and D. Wroblewski. Diagnostics and control in the thermal spray process. *Surf. Coat. Technol.*, 146-147:537–543, 2001.
22. J.R. Fincke, W.D. Swank, and C.L. Jeffrey. Simultaneous measurement of particle size, velocity and temperature in thermal plasmas. *IEEE Trans. Plasma Sci.*, 18:948–957, 1990.
23. S.K. Friedlander. *Smoke, dust and haze: Fundamentals of aerosol dynamics (2nd Ed.)*. Oxford University Press, New York, USA, 2000.
24. A. Gani, P. Mhaskar, and P.D. Christofides. Handling sensor malfunctions in control of particulate processes. *Chem. Eng. Sci.*, 63:1217–1229, 2008.
25. F. Gelbard, and J.H. Seinfeld. Numerical solution of the dynamic equation for particulate processes. *J. Comput. Phys.*, 28:357–375, 1978.
26. L. Gil, and M.H. Staia. Influence of HVOF parameters on the corrosion resistance of NiWCrBSi coatings. *Thin Solid Films*, 420–421:446–454, 2002.
27. E. Hamalainen, J. Vattulainen, T. Alahautala, R. Hernberg, P. Vuoristo, and T. Mantyla. Imaging diagnostics in thermal spraying. “spraywatch” system. In *Thermal spray: Surface engineering via applied research, Proceedings of the international thermal spray conference*, pages 79–83, Montreal, QC, Canada, 2000.

28. T.C. Hanson, and G.S. Settles. Particle temperature and velocity effects on the porosity and oxidation of an HVOF corrosion-control coating. *J. Therm. Spray Technol.*, 12:403–415, 2003.
29. J.A. Hearley, J.A. Little, and A.J. Sturgeon. The effect of spray parameters on the properties of high velocity oxy-fuel NiAl intermetallic coatings. *Surf. Coat. Technol.*, 123:210–218, 2000.
30. H.M. Hulburt, and S. Katz. Some problems in particle technology: A statistical mechanical formulation. *Chem. Eng. Sci.*, 19:555–574, 1964.
31. M. Iovsevic, R.A. Cairncross, and R. Knight. 3D predictions of thermally sprayed polymer splats: Modeling particle acceleration, heating and deformation on impact with a flat substrate. *Int. J. Heat Mass Transfer*, 49:3285–3297, 2006.
32. G.R. Jerauld, Y. Vasatis, and M.F. Doherty. Simple conditions for the appearance of sustained oscillations in continuous crystallizers. *Chem. Eng. Sci.*, 38:1675–1681, 1983.
33. A. Kalani, and P.D. Christofides. Nonlinear control of spatially-inhomogeneous aerosol processes. *Chem. Eng. Sci.*, 54:2669–2678, 1999.
34. A. Kalani, and P.D. Christofides. Modeling and control of a titania aerosol reactor. *Aerosol Sci. Technol.*, 32:369–391, 2000.
35. A. Kalani, and P.D. Christofides. Simulation, estimation and control of size distribution in aerosol processes with simultaneous reaction, nucleation, condensation and coagulation. *Comput. Chem. Eng.*, 26:1153–1169, 2002.
36. O. Knotek, and R. Elsing. Monte carlo simulation of the lamellar structure of thermally sprayed coatings. *Surf. Coat. Technol.*, 32:261–271, 1987.
37. P.A. Larsen, J.B. Rawlings, and N.J. Ferrier. An algorithm for analyzing noisy, in situ images of high-aspect-ratio crystals to monitor particle size distribution. *Chem. Eng. Sci.*, 61: 5236–5248, 2006.
38. K. Lee, and T. Matsoukas. Simultaneous coagulation and break-up using constant-n monte carlo. *Powder Technol.*, 110:82–89, 2000.
39. S.J. Lei, R. Shinnar, and S. Katz. The stability and dynamic behavior of a continuous crystallizer with a fines trap. *AIChE J.*, 17:1459–1470, 1971.
40. M. Li, and P.D. Christofides. Modeling and analysis of HVOF thermal spray process accounting for powder size distribution. *Chem. Eng. Sci.*, 58:849–857, 2003.
41. M. Li, and P.D. Christofides. Feedback control of HVOF thermal spray process accounting for powder size distribution. *J. Therm. Spray Technol.*, 13:108–120, 2004.
42. M. Li, and P.D. Christofides. Multi-scale modeling and analysis of HVOF thermal spray process. *Chem. Eng. Sci.*, 60:3649–3669, 2005.
43. M. Li, and P.D. Christofides. Computational study of particle in-flight behavior in the HVOF thermal spray process. *Chem. Eng. Sci.*, 61:6540–6552, 2006.
44. M. Li, D. Shi, and P.D. Christofides. Diamond jet hybrid HVOF thermal spray: Gas-phase and particle behavior modeling and feedback control design. *Ind. Eng. Chem. Res.*, 43:3632–3652, 2004.
45. M. Li, D. Shi, and P.D. Christofides. Model-based estimation and control of particle velocity and melting in HVOF thermal spray. *Chem. Eng. Sci.*, 59:5647–5656, 2004.
46. M. Li, D. Shi, and P.D. Christofides. Modeling and control of HVOF thermal spray processing of WC-Co coatings. *Powder Technol.*, 156:177–194, 2005.
47. Y. Lin, and E.D. Sontag. A universal formula for stabilization with bounded controls. *Syst. Contr. Lett.*, 16:393–397, 1991.
48. Y.L. Lin, K. Lee, and T. Matsoukas. Solution of the population balance equation using constant-number Monte Carlo. *Chem. Eng. Sci.*, 57:2241–2252, 2002.
49. D.L. Ma, D.K. Tafti, and R.D. Braatz. Optimal control and simulation of multidimensional crystallization processes. *Comput. Chem. Eng.*, 26:1103–1116, 2002.
50. A. Martinez, C. Gonzalez, M. Porras, and J.M. Gutierrez. Nano-sized latex particles obtained by emulsion polymerization using an amphiphilic block copolymer as surfactant. *Colloids and Surfaces A: Physicochemical and Engineering Aspects*, 270–271:67–71, 2005.
51. P. Mhaskar, A. Gani, C. McFall, P.D. Christofides, and J.F. Davis. Fault-tolerant control of nonlinear process systems subject to sensor faults. *AIChE J.*, 53:654–668, 2007.

52. S.M. Miller, and J.B. Rawlings. Model identification and control strategies for batch cooling crystallizers. *AIChE J.*, 40:1312–1327, 1994.
53. J. Mostaghimi, S. Chandra, R. Ghafouri-Azar, and A. Dolatabadi. Modeling thermal spray coating processes: a powerful tool in design and optimization. *Surf. Coat. Technol.*, 163-164: 1–11, 2003.
54. D. Ramkrishna. The status of population balances. *Rev. Chem. Eng.*, 3:49–95, 1985.
55. J.B. Rawlings, S.M. Miller, and W.R. Witkowski. Model identification and control of solution crystallization process – a review. *Ind. Eng. Chem. Res.*, 32:1275–1296, 1993.
56. J.B. Rawlings, C.W. Sink, and S.M. Miller. Control of crystallization processes. In *Industrial crystallization - theory and practice*, pages 179–207, Butterworth, Boston, 1992.
57. S. Rohani, and J.R. Bourne. Self-tuning control of crystal size distribution in a cooling batch crystallizer. *Chem. Eng. Sci.*, 12:3457–3466, 1990.
58. D. Semino, and W.H. Ray. Control of systems described by population balance equations-I. controllability analysis. *Chem. Eng. Sci.*, 50:1805–1824, 1995.
59. D. Semino, and W.H. Ray. Control of systems described by population balance equations-II. emulsion polymerization with constrained control action. *Chem. Eng. Sci.*, 50:1825–1839, 1995.
60. D. Shi, N.H. El-Farra, M. Li, P. Mhaskar, and P.D. Christofides. Predictive control of particle size distribution in particulate processes. *Chem. Eng. Sci.*, 61:268–281, 2006.
61. D. Shi, M. Li, and P.D. Christofides. Diamond jet hybrid HVOF thermal spray: Rule-based modeling of coating microstructure. *Ind. Eng. Chem. Res.*, 43:3653–3665, 2004.
62. D. Shi, P. Mhaskar, N.H. El-Farra, and P.D. Christofides. Predictive control of crystal size distribution in protein crystallization. *Nanotechnology*, 16:S562–S574, 2005.
63. T. Smith, and T. Matsoukas. Constant-number Monte Carlo simulation of population balances. *Chem. Eng. Sci.*, 53:1777–1786, 1998.
64. W.J. Stark, A. Baiker, and S.E. Pratsinis. Nanoparticle opportunities: pilot-scale flame synthesis of vanadia/titania catalysts. *Part. Part. Syst. Charact.*, 19:306–311, 2002.
65. W.D. Swank, J.R. Fincke, D.C. Haggard, G. Irons, and R. Bullock. HVOF particle flow field characteristics. In *Thermal spray industrial applications, Proceedings of the 7th national thermal spray conference*, pages 319–324, Boston, Massachusetts, 1994.
66. Tecnar Automation. *DPV-2000 Reference Manual*.
67. E. Turunen, T. Varis, S.-P. Hannula, A. Vaidya, A. Kulkarni, J. Gutleber, S. Sampath, and H. Herman. On the role of particle state and deposition procedure on mechanical, tribological and dielectric response of high velocity oxy-fuel sprayed alumina coatings. *Mat. Sci. Eng. A*, 415:1–11, 2006.
68. P.G. Vekilov, and F. Rosenberger. Dependence of lysozyme growth kinetics on step sources and impurities. *J. Cryst. Growth*, 158:540–551, 1996.
69. J. Wilden, J.P. Bergmann, and T. Luhn. Aspects of thermal spray molding of micro components. In *Thermal spray: Science, innovation, and application, Proceedings of the 2006 international thermal spray conference*, pages 1243–1246, Seattle, WA, 2006.
70. W. Xie, S. Rohani, and A. Phoenix. Dynamic modeling and operation of a seeded batch cooling crystallizer. *Chem. Eng. Comm.*, 187:229–249, 2001.
71. D. Zhang, S.J. Harris, and D.G. McCartney. Microstructure formation and corrosion behaviour in HVOF-sprayed Inconel 625 coatings. *Mat. Sci. Eng. A*, 344:45–56, 2003.
72. G.P. Zhang, and S. Rohani. On-line optimal control of a seeded batch cooling crystallizer. *Chem. Eng. Sci.*, 58:1887–1896, 2003.



<http://www.springer.com/978-1-4419-5831-0>

Feedback Control of MEMS to Atoms

Gorman, J.J.; Shapiro, B. (Eds.)

2012, VIII, 384 p., Hardcover

ISBN: 978-1-4419-5831-0